Why plants make puzzle cells, and how their shape emerges

Aleksandra Sapala[1,8], Adam Runions[1,2,8], Anne-Lise Routier-Kierzkowska[1,3], Mainak Das Gupta[1,4], Lilan Hong[5], Hugo Hofhuis[1], Stéphane Verger[6] , Gabriella Mosca[1], Chun-Biu Li[7] , Angela Hay[1], Olivier Hamant[6], Adrienne H. K. Roeder[5], Miltos Tsiantis[1], Przemyslaw Prusinkiewicz[2], Richard S. Smith[1,9]

[1] Department of Comparative Development and Genetics, Max Planck Institute for Plant Breeding Research, Cologne, 50829 Germany

[2] Department of Computer Science, University of Calgary, Calgary, AB T2N 1N4 Canada

[3] Current address: Institut de Recherche en Biologie Végétale, Université de Montréal, Montréal, QC H1X 2B2 Canada

[4] Department of Microbiology and Cell Biology, Indian Institute of Science, Bangalore, Karnataka, 560012 India

[5] Weill Institute for Cell and Molecular Biology and School of Integrative Plant Science, Section of Plant Biology, Cornell University, Ithaca, NY 14850 USA

[6] Laboratoire Reproduction et Développement des Plantes, Univ Lyon, ENS de Lyon, UCB Lyon 1, CNRS, INRA, F-69342, Lyon, France

[7] Department of Mathematics, Stockholm University, 106 91 Stockholm, Sweden

[8] These authors contributed equally

[9] Lead contact: smith@mpipz.mpg.de

ABSTRACT

The shape and function of plant cells are often highly interdependent. The puzzle-shaped cells that appear in the epidermis of many plants are a striking example of a complex cell shape, however their functional benefit has remained elusive. We propose that these intricate forms provide an

effective strategy to reduce mechanical stress in the cell wall of the epidermis. When tissue-level growth is isotropic, we hypothesize that lobes emerge at the cellular level to prevent formation of large isodiametric cells that would bulge under the stress produced by turgor pressure. Data from various plant organs and species support the relationship between lobes and growth isotropy, which we test with mutants where growth direction is perturbed. Using simulation models we show that a mechanism actively regulating cellular stress plausibly reproduces the development of epidermal cell shape. Together, our results suggest that mechanical stress is a key driver of cell-shape morphogenesis.

KEYWORDS

pavement cells, morphogenesis, organ shape, growth, modelling, plant development

INTRODUCTION

During growth and morphogenesis, plant cells undergo dramatic changes in size and shape. Starting from small isodiametric cells in proliferative tissues, cells stop dividing and can expand to over 100 times their original size. This results in large elongated cells, such as those in roots and stems, or much more intricate forms, such as the jigsaw puzzle-shaped epidermal cells of *Arabidopsis thaliana* leaves (Fig. 1A), which we call puzzle cells. The processes underlying the formation of these cells are presently unclear, and it has been proposed that they emerge from either the localized outgrowth of lobes (also called protrusions) (Fu et al., 2002; Mathur 2006; Xu et al., 2010; Zhang et al., 2011), localized restriction of indentations (Fu et al., 2009; Sampathkumar et al., 2014; Lin et al., 2013), or a combination of both (Fu et al., 2005; Abley et al., 2013; Armour et al., 2015, Higaki et al., 2016, Majda et al., 2017). Specific members of the Rho GTPase of plants (ROP) family of proteins play a key role in shaping these cells. ROP2 and ROP6 mutually inhibit each other's

49 accumulation at the plasma membrane, creating a co-repression network that divides the plasma
50 membrane into alternating expression domains, with ROP2 in lobes and ROP6 in indentations (Fu
51 et al., 2009). These proteins are thought to regulate pavement cell interdigitation through their
52 interactions with RIC proteins, with ROP2 recruiting actin through RIC4 in the lobes, and ROP6
53 recruiting cortical microtubules through RIC1 and katanin to restrict growth in indentations.
54 Disruptions in the ROP/RIC pathways lead to defects in puzzle cell formation (Fu et al., 2002; Fu et
55 al., 2005; Fu et al., 2009; Xu et al., 2010; Lin et al., 2013). Since a lobe in one cell must be
56 matched by an indentation in its neighbor, some manner of extracellular communication is required.
57 The plant hormone auxin has been proposed to act as this signal (Fu et al., 2005; Xu et al., 2010; Li
58 et al., 2011), although recent data call for a re-evaluation of this hypothesis (Gao et al., 2015,
59 Belteton et al., 2017).

60 Although these studies have elucidated many of the molecular players involved in puzzle cell
61 patterning, a mechanistic theory is lacking, in part because the function of the puzzle-shape in
62 epidermal cells is unclear (Bidhendi and Geitmann, 2017). It has been hypothesized that the
63 interdigitation of the lobes and indentations may strengthen the leaf surface (Glover 2000; Jacques
64 et al., 2014; Sotiriou et al., 2018), with material sciences studies supporting the plausibility of this
65 idea (Lee et al., 2000). Alternatively, puzzle-shaped cells may allow for the correct spacing of the
66 other epidermal cell types, such as guard cells and stomata (Glover et al., 2000). However there is
67 little experimental support for these hypotheses at present. Here we propose a different function for
68 the puzzle shape, that it is an adaptation to a developmental constraint related to the mechanical
69 forces that act on turgid plant cells that reside in the epidermis.

70 Mechanically, plant cells are like small balloons inflated with considerable turgor pressure, up to 10
71 bar in *Arabidopsis* leaf cells (Forouzesh et al., 2013), reaching values as high as 50 bar in
72 specialized cells such as stomata (Franks et al., 2001). Turgor pressure induces mechanical stress in
73 the cell wall, which is the ratio of the force acting on a cross-section of the material (cell wall)

74 scaled by the area of the material resisting the force. If the wall is made of a homogeneous
75 material, then for a given turgor pressure, cell size and shape provide a good predictor of
76 mechanical stress (Niklas 1992; Geitmann & Ortega 2009), with larger cells subject to more stress
77 than smaller ones (Bassel et al., 2014). Although the composition of the cell wall is undoubtedly
78 more complex than this (reviewed by Cosgrove, 2005, Cosgrove 2014), this suggests that cell shape
79 and mechanical stress are intimately connected. Most plant tissues emerge from undifferentiated
80 cells that are initially small and isodiametrically shaped, and subsequently proliferate, differentiate
81 and expand. For epidermal cells composing the outermost cell layer in each organ, minimizing
82 mechanical stress on their walls is likely particularly important as the epidermis limits organ growth
83 and is under tension from internal tissues (Savaldi-Goldstein et al., 2007; Kutschera & Niklas 2007;
84 Beauzamy et al., 2015).

85 Here we explore the relationship between cell shape and mechanical stress, to understand if
86 mechanical stress is a morphological constraint in shaping epidermal cells. We propose a plausible
87 driver for the creation of the intricate, commonly observed cell forms by demonstrating that they
88 reduce the forces the cell wall has to withstand. We present computer simulation models that show
89 that actively minimizing force leads to the emergence of the puzzle cell shape, reducing stress and
90 thus potentially lowering the amount of cellulose and other wall material required to maintain
91 mechanical integrity of the cell wall.

92

93 **RESULTS**

94 **Cell shape predicts mechanical stress magnitude**

95 Using the Finite Element Method (FEM), we performed simulations on single cells with idealized
96 shapes to explore the effect of cell shape on turgor-induced mechanical stresses (more precisely, the
97 trace of the Cauchy stress tensor) in the cell wall (Bassel et al., 2014). To access basic relations

98 between cell shape and stress we used uniform, isotropic elastic properties for cell walls, which
99 were assumed to have cell wall thickness of 1 µm, and pressurized the cells to 5 bar (note that this
100 neglects inhomogeneities in the cell wall, as have been observed by Majda et al. (2017)). Starting
101 with a small cube-shaped cell (10x10x10 µm) we increased the initial cell size in different
102 dimensions to observe the effect on stress following pressurization. We observed that an increase of
103 cell length in one direction (50x10x10 µm) does not significantly increase maximal stress in the cell
104 wall (Fig. 1B). This suggests that anisotropic growth that results in long thin cells is a mechanically
105 advantageous strategy to limit stress magnitude, limiting the wall thickness required to maintain the
106 cell's integrity. Next, we simulated a cell expanded in two directions (50x50x10 µm) and observed
107 that the maximal stress was much higher. Enlarging the cell in two directions created a large open
108 surface area, causing the cell wall to bulge out in response to turgor pressure, greatly increasing the
109 stress. When the third dimension is enlarged to form a cube (50x50x50 µm), only a small increase
110 in maximal stress is observed compared to the 50x50x10 µm case. Thus if a cell must increase its
111 size, an effective way to do it without increasing stress is to elongate along a single axis, instead of
112 expanding in two or three dimensions. Plant organs such as roots, hypocotyls, sepals, many grass
113 leaves and stems grow primarily in one direction and have elongated cells, which would maintain
114 low stress during growth. But how do cells avoid excessive stress if they are part of a tissue that
115 grows in two directions, such as the surface of broad leaves?

116 Here we propose that the puzzle cell shape, with lobes and indentations, provides a solution to this
117 problem. To test this hypothesis, we began by analyzing the stress in a mechanical model of the
118 cotyledon epidermis of *Arabidopsis thaliana.* A cellular surface mesh was extracted from confocal
119 images using the image analysis software MorphoGraphX (Barbier de Reuille et al., 2015). The
120 mesh was then extruded to form a layer of 3D cells of uniform thickness representing the cotyledon
121 epidermis (Mosca et al., 2017). Next, the cells were pressurized, and the stresses visualized (Fig.
122 1C, F). In order to examine the effect of lobes on the stress, we created a second template with

123 simplified cell shapes using only the junctions (points shared by three different cells) of the original
124 cells (Fig. 1D). While the total and average cell area in the original and simplified tissue is the
125 same, the overall stress is much lower in the original (puzzle-shaped) tissue, especially for large
126 cells (Fig. 1 C, D).

127 Next, we asked how the presence of lobes affects mechanical stress in the cell wall. We computed
128 mechanical stress in idealized circular cells, adding protrusions to simulate the lobes of a puzzle
129 cell. While stress increases with diameter (Fig. 1E), adding lobes to the original cell does not
130 significantly affect stress in the central part of the cell. Furthermore, increasing lobe length has no
131 impact on stress, although the total volume of the cell increases. Similarly, changing lobe width or
132 number does not affect stress in the cell center (Fig. 1E, inset). However, there are stress hot spots
133 located between the protrusions, where values appear to be inversely correlated with the width of
134 the protrusion (the distance between the flanks of two consecutive lobes), and increase with the
135 radius of the central part of the cell. This is similar to what we observed in pressurized puzzle cells
136 (Fig. 1C, F). In both cases, high stress values appear in open areas and in the indentions between
137 protrusions, consistent with previous observations (Sampathkumar et al., 2014). In the absence of
138 lobes, the load acting in the middle of the cell is transmitted approximately evenly to the cell
139 contour, whereas in puzzle-shaped cells, the central load is transferred to the area between the lobes,
140 creating stress hot spots in the indentations. The magnitude of stress in the indentations is therefore
141 a direct reflection of the large open areas of the cell that they support, and is thus higher when cells
142 bulge more. Despite the stress hot spots between protrusions, overall stress at both the cell and
143 tissue level is much lower in puzzle shaped cells than in the simplified cell shape template (Fig. 1C,
144 D).

145 Following these observations, we propose that mechanical stress in both puzzle-shaped and non-
146 lobed cells is approximated by the size of the largest empty circle (LEC) that can fit into the cell
147 contour (Fig. 1G, yellow). For long thin cells, such as in roots or stems, the size of the empty circle

is the cell diameter, which is known to predict stress for cylindrical cells (Geitmann & Ortega 2009). We hypothesize that in a strongly anisotropically growing organ the plant would make long thin cells, whereas in more isotropic organs puzzle cells would be produced. Counter-intuitively, it is the requirement for isotropic expansion at the tissue scale that drives the irregular shape of puzzle cells.

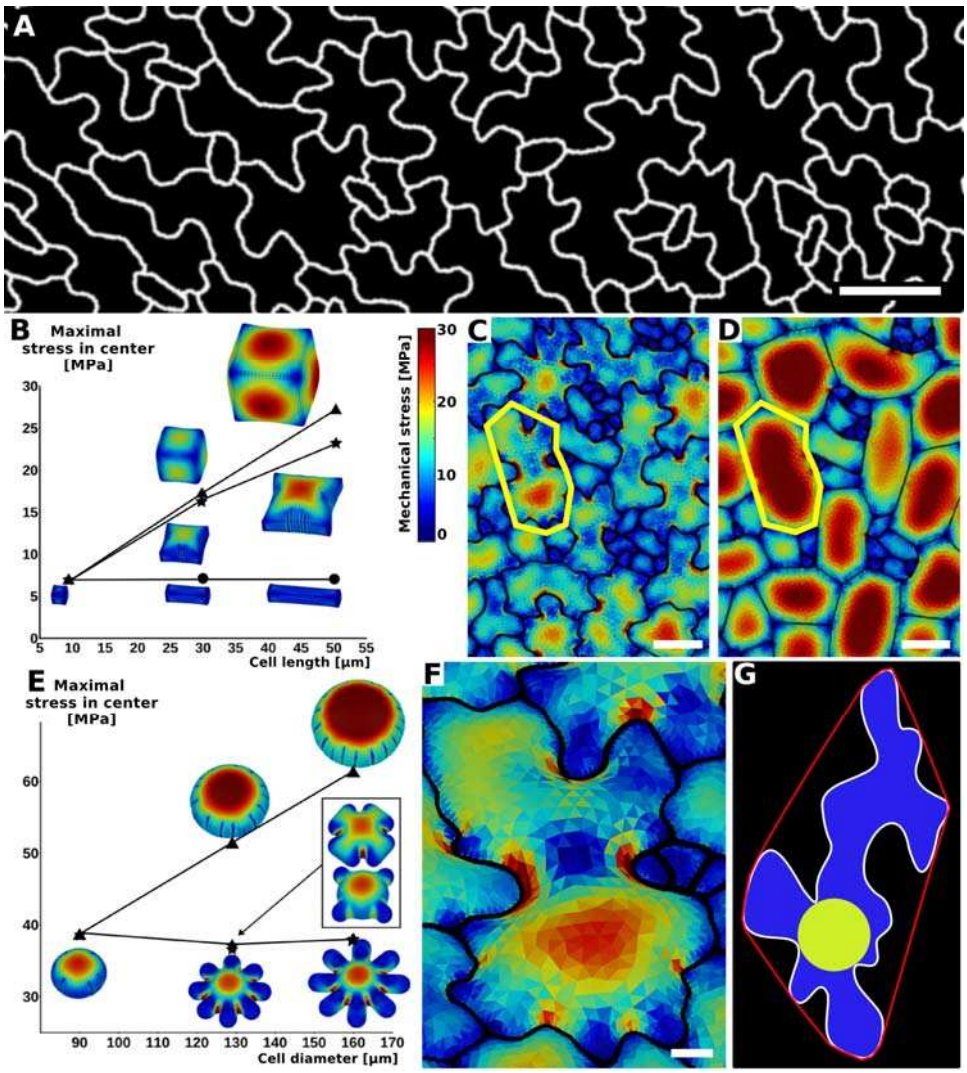

Figure 1. Relationship between cell shape and stress. (A) Cell contours in adaxial epidermis of an *Arabidopsis thaliana* cotyledon. Small, elliptical cells are stomata. Scale bar: 50 µm. (B-F) Cellular stress patterns in finite element method (FEM) simulations. Cell walls have uniform, isotropic material properties (Young's modulus = 300 MPa) and are inflated to the same turgor pressure (5 bar). (B) Graph points show stress in cells expanded in one dimension (circles), two

158 dimensions (stars) or three dimensions (triangles). Enlargement in two or more dimensions
159 substantially increases stress in the center of the cell walls. (C) Principal stresses generated by
160 turgor *in vivo* were simulated in an FEM model on a template extracted from confocal data. (D) A
161 simplified tissue template using the junctions of the cells in (C). The yellow outline marks a
162 corresponding cell in (C) and (D). Total area and number of cells is the same, however the maximal
163 stress is much lower in the puzzle-shaped cells compared to the more isodiametrically-shaped cells.
164 (E) In isolated circular cells, pressure-induced stress increases with diameter (triangles), as was the
165 case in (B). Adding lobes, regardless of their length, width or number (inset) does not influence
166 maximal stress in the cell wall in the center (stars). (F) A close-up view showing high stress areas
167 that coincide with the center of the large open area of the cell, or indentations that support large
168 open areas. (G) Measures used to quantify puzzle cell shape and stress. The largest empty circle
169 (LEC, yellow) that fits inside the cell is a proxy for the maximal stress in the cell wall. The convex
170 hull (red) is the smallest convex shape that contains the cell. The ratio of cell perimeter (white) to
171 the convex hull perimeter gives a measure of how lobed the cell is (termed "lobeyness"). Scale bars:
172 50 µm (C,D), 10 µm (F). Color scale: trace of Cauchy stress tensor in MPa.

173

174 **Cell shape measures**

175 To test our hypothesis, a method to quantify the puzzle shape of cells is required. As the epidermis
176 is a surface of relatively uniform thickness, most shape measures applied to puzzle cells consider
177 only the 2D form of cells, and several methods have been developed for this purpose (see Zhang et
178 al., 2011; Wu et al., 2016, and references therein). A common measure to estimate the complexity
179 of a contour is circularity, indicating how closely a given object resembles a circle. Circularity is
180 calculated using the ratio of the perimeter to the square root of area (Zhang et al., 2011, Majda et
181 al., 2017). However, it is not suitable for our purposes as both simple, elongated cells and lobed

182 puzzle cells have increased circularity values. Consequently, it cannot be used to reliably
183 distinguish between these cell shapes. Another common approach is to calculate a skeleton based on
184 the cell contour and count its branches (Le et al., 2006). Unfortunately skeletonization methods can
185 be very sensitive to small changes in shape (such as the error produced by discretization) making it
186 difficult to robustly quantify the geometric features of cells.

187 Here we use a method based on the convex hull (Wu et al., 2016), the smallest convex shape
188 containing the cell (think of a rubber band surrounding the cell). We define cell *lobeyness* as the
189 perimeter of the cell divided by the perimeter of its convex hull (Fig. 1G, white and red,
190 respectively). The higher this value, the more lobed the cell is expected to be. The ratio of the cell's
191 convex hull area to that of the cell is another possibility, however we found that for important
192 special cases, such as worm-shaped or boomerang-shaped cells, using the area may produce high
193 ratios even when cells do not have significant lobes. The ratio of perimeters (perimeter of the cell /
194 perimeter of its convex hull) is less affected in these cases.

195

196 A mechanistic model of puzzle shape emergence

197 Cortical microtubules are thought to direct the deposition of cellulose fibrils in the cell wall (Green
198 1962; Paredez et al., 2006). These fibrils stiffen the cell wall, causing growth to be favored in the
199 direction perpendicular to the fibrils (Suslov & Verbelen 2006). Cortical microtubules have also
200 been shown to orient along the maximal direction of tensile stress (Hejnowicz et al., 2000; Hamant
201 et al., 2008). The fact that growth anisotropy affects cell shape and cell shape affects stress,
202 suggests a feedback mechanism linking cell shape and growth *via* the response of cortical
203 microtubules to mechanical stress directions. This idea is supported by experimental and modeling
204 work showing that predicted stress directions in puzzle cells align with cortical microtubule
205 direction in *Arabidopsis* cotyledons (Sampathkumar et al., 2014).

206 Here we propose a dynamic simulation model of puzzle cell patterning based on the idea that cells
207 can respond to mechanical signals generated by cell geometry. The model focuses on the
208 developmental stage when cells stop dividing and begin to expand. The basic principle behind the
209 model is that as cells grow, stresses gradually increase, and when they reach a threshold level the
210 cell wall is reinforced to resist these stresses. Using simulations on idealized cell templates, we test
211 whether that basic principle is sufficient to generate different cell shapes, depending on the
212 anisotropy of tissue growth. The emerging cell shapes primarily arise from the growth direction
213 imposed at the tissue level that is locally modulated by stress-based growth restriction.

214 We present the essential aspects of the model here (Fig. 2), but refer the reader to the Appendix for
215 further details. Cells are represented as polygons (Fig. 2A), with wall segments between nodes
216 acting like linear springs (Prusinkiewicz and Lindenmayer, 1990), and nodes having resistance to
217 bending between adjoining segments (Matthews, 2002). Thereby the model accounts for cell wall
218 thickness and penalizes sharp features, which are usually not observed in nature. A simulation step
219 consists of 3 phases (Fig. 2B,C). During the first phase, springs are inserted across cells in addition
220 to those defining the cell polygon. These additional springs account for the presence of oriented cell
221 wall stiffening components, such as cellulose microfibrils whose deposition is guided by cortical
222 microtubules (Paredez et al., 2006) that are thought to respond to stress (Hejnowicz et al.,2000;
223 Hamant et al.,2008). The springs also only exert force when they exceed a given target length,
224 related to the LEC, which provides a proxy for stress (Fig. 1). These connections across the cells
225 introduce growth restrictions into the model, and are placed according to two criteria. First, these
226 springs connect each node to the closest node across the cell falling within a given angle from the
227 normals of the two nodes. Second, connections are inhibited if the the cell wall is convex (see
228 Appendix, sec. 2.3; Fig. 2 – figure supplement 1). This facilitates lobe formation, gives a pattern
229 that both follows the patterns of stress previously reported by Sampathkumar et al. (2014) and is
230 consistent with the proposed action of ROP2 in excluding ROP6 from lobes. In the second phase,

growth is simulated by displacing the wall segments, based on the specified tissue growth (e.g. isotropically or anisotropically), and relaxing cell wall springs so that the rest lengths match their actual length. The connections across the cells do not grow. Once placed, their reference length is unaffected by growth and is fixed until the connection is removed. In the third and final phase, a new resting state is found by updating cell shapes to achieve mechanical equilibrium. The next simulation step commences by reassigning microtubule/cellulose connections based on the new cell shape and updating the rest-length of cell wall segments. This highly dynamic arrangement of microtubules is consistent with a similar assumption underlying mechanistic explanations of cell division patterns (Lloyd 1991, Besson and Dumais 2011).

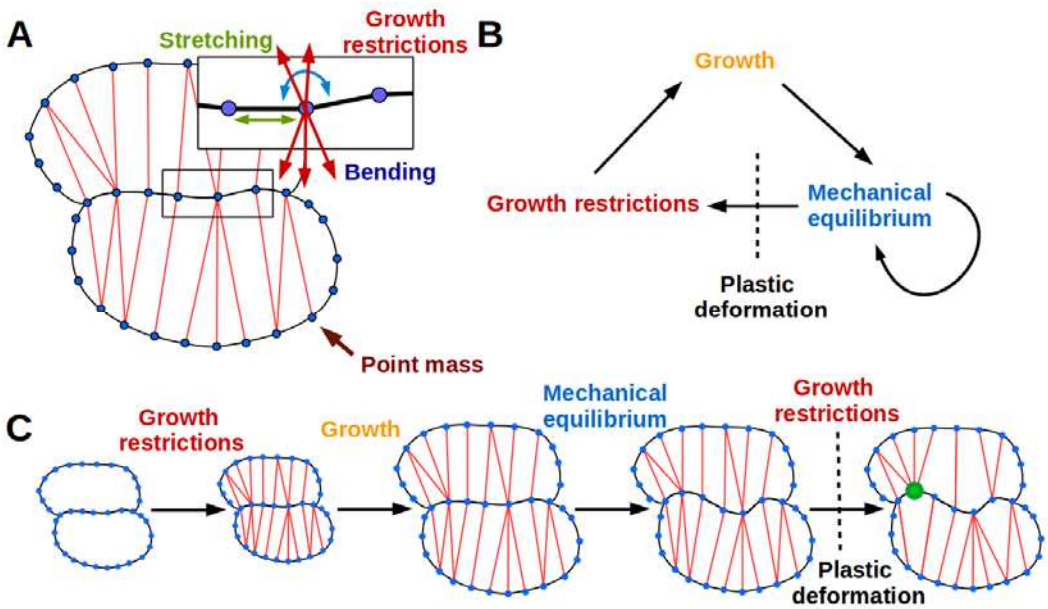

Figure 2. The 2D puzzle cell model. (A) Mechanical representation of cells. Cell walls are discretized into a sequence of point masses (blue circles) connected by linear wall-segments (white lines). Growth restricting connections (red lines) join point masses across the cell. The forces acting on the point mass are produced by stretching of wall segments and growth restricting connections as well as bending of the cell wall at the mass. (B-C) The simulation loop consists of 3 steps (B), as depicted for a diagrammatic example in (C). Step 1: additional transversal springs (red) are added to the model to represent oriented cell wall stiffening components guided by microtubules connecting

247 opposing sides of the cell. They act like one-sided springs in that they exert a force when under
248 tension (i.e. stretched beyond their rest length), but are inactive when compressed. This is
249 consistent with the high tensile strength of cellulose. Step 2: the tissue is scaled to simulate growth,
250 which can have a preferred direction (i.e. is anisotropic). Step 3: the network of springs reaches
251 mechanical equilibrium. Transversal springs restrict cell expansion in width, causing cell walls to
252 bend. Before the next iteration, wall springs are relaxed and transversal springs are rearranged to
253 reflect the new shape of cells. Cell shapes emerging in the model are determined by the nature of
254 the assumed tissue growth direction. Note that in (C) the deformation of the cell causes the
255 placement of growth restrictions to change during the subsequent iteration, where the green mass at
256 the lobe tip attracts more connections on the convex side and loses connections on the concave side.

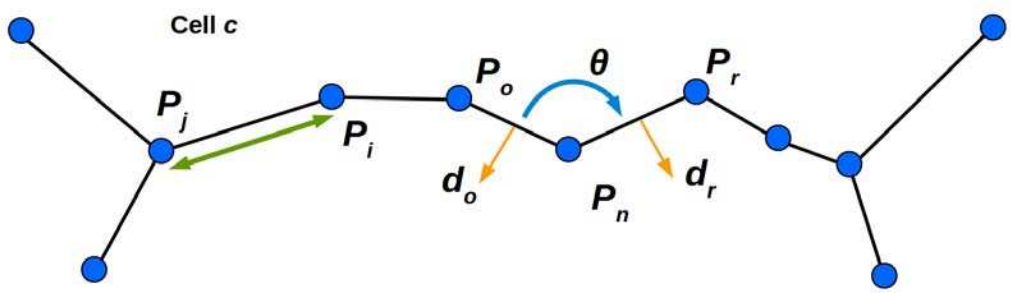

257 **Figure 2 – figure supplement 1. Mechanical properties of the cell wall are simulated using**
258 **stretching and bending springs.** See Appendix sec. 2.5 for details. The linear spring connecting
259 masses m_i and m_j is shown, and generates a force parallel to the line connecting their positions P_i
260 and P_j (green line with arrowheads). The bending spring in cell c at mass m_n generates a force
261 acting on m_n and the neighboring masses m_o and m_r. The sign and magnitude is determined by θ (the
262 signed angle between P_o and P_r). The vector d_o (the outward facing normal to the cell wall spanning
263 P_n and P_o) determines the direction of the force acting on mass m_o. The vector d_r is defined
264 similarly, and determines the direction of the force acting on m_r. The force acting on mass m_n
265 balances those acting on masses m_o and m_r.

266

267 If tissue growth is isotropic, cells quickly approach their target LEC, and connections representing
268 the cellulose and microtubules begin to stretch. Lobes emerge as the indentations (concave regions)
269 attract more connections and protrusions (convex regions) lose connections (Fig. 2C, Movie 1). The
270 increased number of connections at indentations is an emergent geometric effect. As the indentation
271 deepens, and its tip becomes more exposed, it becomes the closest node to a larger number of nodes
272 on the opposing cell wall, thus attracting more connections. This is consistent with the findings of
273 Sampathkumar et al. (2014), who detected oriented patterns of mechanical anisotropy with atomic
274 force microscopy, consistent with the proposed directed accumulation of cellulose microfibrils in
275 the indentations of puzzle cells. These connections act as a proxy for the additional stress in the
276 indentations (Fig. 1). Interestingly, the accumulation of connections in the indentations is consistent
277 with the observed auto-catalytic effect of microtubule bundling in indentations in real pavement
278 cells, *via* induced ROP6/RIC1/katanin-dependent microtubule severing activity (Lin et al.,2013;
279 Sampathkumar et al., 2014). Conversely, protrusions gradually lose connections as neighboring
280 nodes become closer to opposing portions of the cell wall. This is enhanced by the model
281 assumption that connections cannot be made across the cell to opposite walls from regions that are
282 too convex (i.e. in the lobes, Fig. 3A,D). If the simulation is performed with anisotropic growth, the
283 cellulose-microtubule connections are never stretched significantly beyond the LEC, and cells
284 simply elongate, and lobes do not emerge (Fig. 3B, E). In other words, stress-based activation of
285 connections induces indentations, coinciding with locations of ROP6 activity, which necessarily
286 generate incipient lobes in adjacent portions of the cell-wall where ROP2 is localized, accentuating
287 their outgrowth. Thus, although phrased in geometric terms, our model is consistent with both the
288 antagonistic local molecular interactions of ROP2-ROP6 and the stress-based feedbacks proposed
289 by Sampathkumar et al.,(2014).

290 The main parameters of the model are the stiffness of the cell walls and the cellulose-microtubule
291 connection springs, the angle within which connections can be made, and the convexity criteria for

292 attachment to the opposing wall (see Appendix Table 1 for all parameter values). To examine the
293 contribution of growth distribution to cell shape we varied growth anisotropy while all other model
294 parameters remained constant (Fig. 3A-C). In this case, the emergence of puzzle vs. elongated cells
295 depends only on the anisotropy of growth at the tissue scale, with puzzle cells appearing for
296 isotropic growth, and elongated cells for anisotropic growth (Movie 1, Movie 2). If the growth
297 specified has a gradient of anisotropy at tissue scale, a gradient of cell shapes from elongated to
298 lobed is produced (Movie 3). Similar gradients in cell shape are seen in *A. thaliana* leaves, where
299 elongated cells cover the anisotropically growing midrib, whereas lobed cells adorn the adjacent
300 isotropically growing leaf blade (Fig. 3C).

301 To explore the effect of model parameters on cell-morphology we performed a parameter space
302 exploration using the simulation with isotropic growth as a reference (Fig. 3A). We varied isotropy
303 within a range of 40%-100% of the reference value and all other parameters within a range of at
304 least 25%-200% (Fig. 3 – figure supplement 1, Movies 5-10). This exploration showed that when
305 growth is anisotropic, there is no strict 'threshold' for the onset of lobing, but rather it is a
306 continuous characteristic. This feature is preserved when the initial template and additional
307 parameters are varied (Fig. 3 – figure supplement 2). Parameter variation also demonstrates that the
308 model can generate a diverse range of plausible cell shapes, similar to those observed in nature (e.g.
309 Fig. 3 – figure supplement 2B 60% isotropy; which are reminiscent of epidermal cells in maize
310 leaves).

311 To validate the model, we confirmed in a FEM analysis that limiting the size of the LEC by creating
312 lobes during growth reduces the cellular stress (Fig. 3F-G). This causes the maximum stress in
313 simulated tissues to plateau, greatly reducing it compared to isodiametric cells of the same size (Fig.
314 3H). The model thus illustrates how a mechanism actively limiting the mechanical stress of cells by
315 restricting large open areas (LECs) can lead to the formation of puzzle-shape cells in the context of
316 isotropic growth.

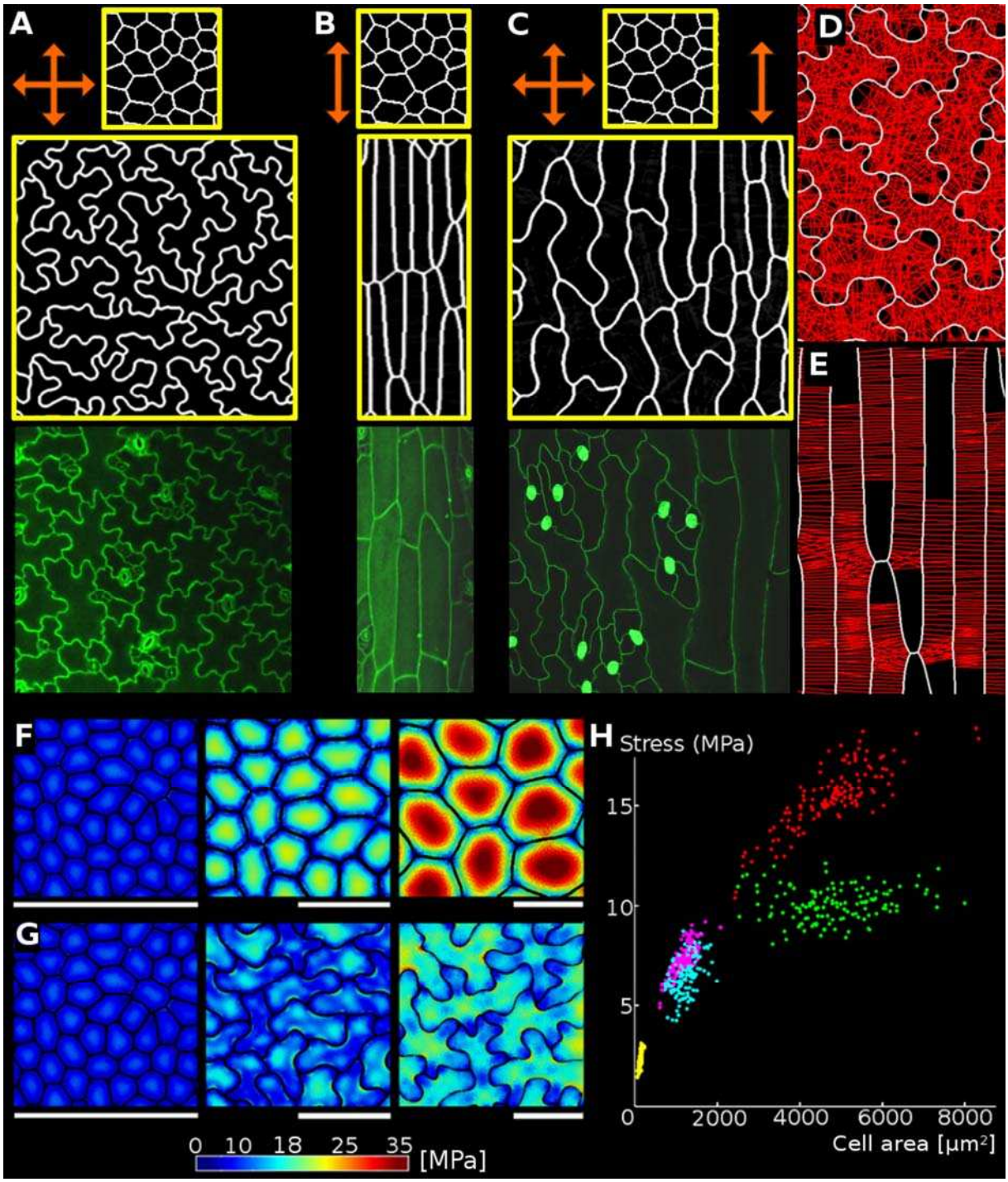

Figure 3. Geometric-mechanical model of puzzle cell emergence. (A) Starting with meristematic-like cells (top), growing the tissue isotropically, i.e. equally in all directions (arrows), produces puzzle-shaped cells (middle) that resemble cotyledon epidermal cells (bottom). (B) Growing the tissue frame primarily in one direction (anisotropically) results in elongated cells (middle) as observed, for example, in the petiole (bottom). (C) A gradient of growth anisotropy

322 (increasing left to right) produces a spatial gradient of cell shapes (middle), as observed between the
323 blade and midrib of a leaf (bottom). (D-E) Connections of transversal springs (red) restricting
324 growth in each simulation step in tissues with isotropic (D) and anisotropic (E) growth. To make
325 connections more apparent, only 50% are visualized. (F-G) Cell outlines from 2D models with
326 isotropic growth were used to generate 3D templates for FEM models (growth progresses from left
327 to right, scale bars: 80 μm). (F) As the tissue grows, cells lacking transversal springs conserve
328 their original shape. In pressurized cells, mechanical stress increases with the cell size. (G) When
329 transversal springs are added, tissue expansion generates lobed cells. (H) Average stress in the cell
330 increases with cell area in the polygonal cells (yellow, pink, red), while stress plateaus during tissue
331 grows when cells form lobes (cyan, green). Color scale: trace of Cauchy stress tensor in MPa.

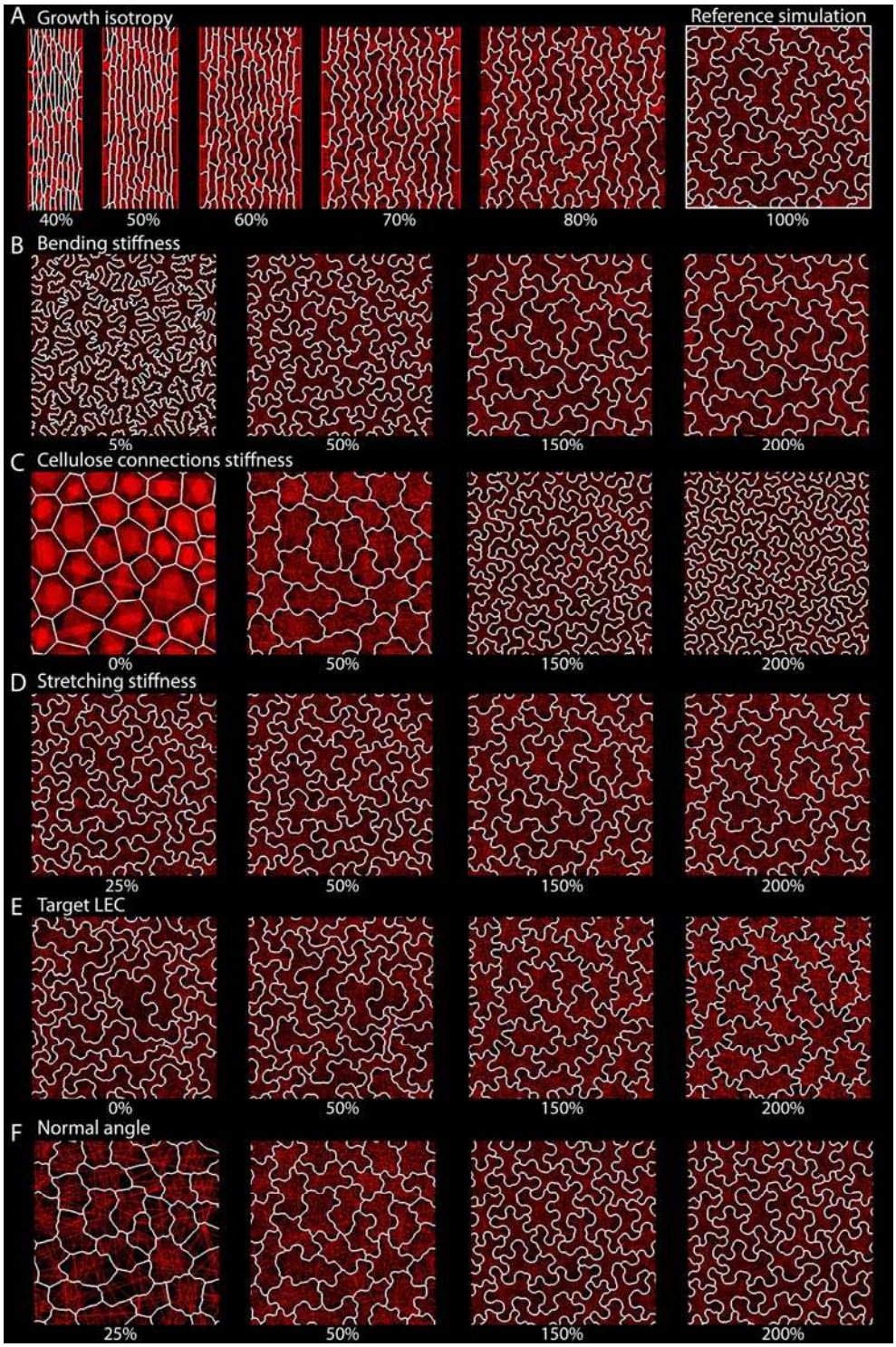

Figure 3 – figure supplement 1. Parameter space exploration for key model parameters. The wild type isotropic simulation was used as the reference simulation (A, 100%), and parameters were varied independently. Isotropy was varied from 40% to 100% of the reference value and all other parameters were varied from (at least) 25% to 200%. Snapshots of the final stage of each simulation

336 are displayed. The varied parameters were: (A) growth isotropy (growth in width vs growth in
337 length), (B) bending stiffness, (C) cellulose connection stiffness, (D) stretching stiffness, (E) target
338 LEC, (F) normal angle.

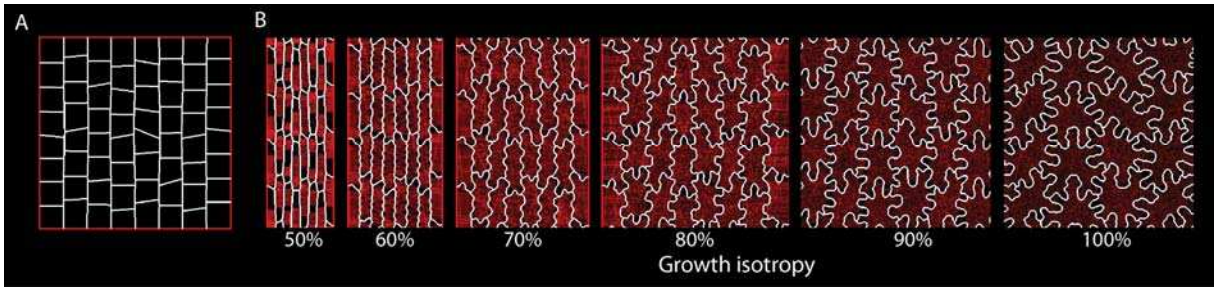

339 **Figure 3 – figure supplement 2. Varying isotropy for an alternative parameter set.** Using a
340 different parameter set compared to Figure 3 – figure supplement 1A, growth isotropy was varied
341 while all other parameters were constant. Compared to Figure 3 – figure supplement 1A, target LEC
342 has been increased by 100%, simulation time extended by 10%, and the initial cellular was changed
343 to that shown in (A). (B) Snapshots of the final stage of each simulation as isotropy (growth in
344 width vs growth in length) was varied from 50% to 100% Although cell morphology changes, the
345 relation between isotropy and puzzle-cell development is maintained.

346

347 The model relies on cell-autonomous mechanical restriction of indentations through controlled
348 cellulose deposition and does not require cell-cell signaling molecules to synchronize the
349 indentations in one cell with the protrusions of its neighbor. Nonetheless, synergies exist between
350 the mechanical and biochemical control of cell morphogenesis. In particular, the ROP6 in the
351 indentation of one cell must coincide with ROP2 in the corresponding lobe of the neighboring cell.
352 Although biochemical signals cannot be ruled out (Xu et al., 2010), our model predicts that this
353 signal could be passed through the geometry of the cells *via* its effect on stress patterns or geometry,
354 with indentations attracting microtubule-cellulose deposition and ROP6, and lobes suppressing
355 microtubules *via* the cell-autonomous co-repression of ROP2 and ROP6.

356

357 **Isotropic tissue growth is correlated with puzzle-shaped cell formation**

358 Our model predicts that puzzle cells should appear when cells stop dividing and tissue growth is not
359 primarily in one direction. To test this prediction experimentally, we performed time-lapse confocal
360 imaging on cotyledons (n=3 time-lapse series), which have a blade of roughly isodiametric shape,
361 growing from 2 to 4 days after germination (DAG). Epidermal cells of *Arabidopis thaliana*
362 cotyledons begin to acquire a puzzle-shaped morphology roughly 2 DAG, whereas the organ
363 achieves its characteristic round shape at approximately 3 DAG, long before reaching its final size
364 (Zhang et al., 2011). We used MorphoGraphX (Barbier de Reuille et al., 2015) to extract growth
365 rates and directions, and these results confirm that the overall growth of cotyledon is isotropic as
366 suggested by its round shape. To examine the correlation between growth anisotropy and lobeyness
367 we pooled the data from the final time-point of our time-lapse series. We then extracted the largest
368 100 cells from this set (i.e. those most likely to be affected by the stress-minimizing mechanism)
369 and found a significant correlation between growth anisotropy and lobyness (Pearson correlation
370 coefficient $r = -0.46$, $p=0.6 \times 10^{-6}$). Thus, supporting our hypothesis that growth anisotropy and
371 lobeyness are inversely related in the isotropically growing cotyledons of *Arabidopsis* (see also Fig.
372 4A, Fig. 4 - figure supplement 1C).

373 In contrast to cotyledons, the *Arabidopsis* sepal is an elongated organ with epidermal cells that are
374 either small and relatively isodiametric in shape, or large and elongated. Sepals initiate from a band
375 of cells in the floral meristem, undergoing strongly anisotropic growth (Hervieux et al., 2016)
376 which produces giant cells that are far less lobed than those of the cotyledon (compare Fig. 4 -
377 figure supplement 1 A and C). Thus growth isotropy and final organ shape correlate with lobeyness
378 in these two organs.

379 Next we examined cases where genetic modifications changed growth anisotropy and overall organ

380 shape. Sepals of the *ftsh4* mutant show increased variability of organ shape (Hong et al., 2016). In
381 some samples, the growth is more isotropic than wild type, and cells of more isodiametrically
382 shaped organs exhibit decreased growth anisotropy and increased lobeyness, and start to become
383 puzzle shaped (compare Fig. 4 - figure supplement 1 A and B). The shift from anisotropic to
384 isotropic growth in the sepal is thus correlated with a shift from elongated giant cells to puzzle-
385 shaped cells.

386 The opposite change in growth anisotropy and organ shape can be seen in plants overexpressing the
387 *LONGIFOLIA1* (*TRM2*) gene. This causes an elongated cell and organ phenotype in *A. thaliana*
388 cotyledons and leaves (Lee et al., 2006, Drevensek et al., 2012), consistent with effects of a related
389 protein in rice grains (Wang et al., 2015). We created transgenic plants where *LNG1* is
390 overexpressed under the CaMV 35S promoter (*p35S::LNG1*). Our T_1 lines had phenotypes ranging
391 from highly elongated cotyledons and leaves to wild type (Fig. 4C-E). Plants with the elongated
392 phenotype grew more anisotropically than wild type and had epidermal cells with reduced
393 lobeyness (n=3 time-lapse series for each genotype, Fig. 4A-B and F-I). Thus the change in growth
394 and organ shape from isodiametric to elongated correlated with a decrease in cell lobeyness.

395 To further test the generality of the correlation between organ shape and cell shape, we examined
396 fruit epidermal cells in a sample of 21 species from the Brassicaceae family (full dataset shown in
397 Hofhuis and Hay, 2017). These fruit pods were either elongated siliques or short, rounded silicles
398 and we only observed puzzle-shaped cells in silicles, not in siliques (Fig. 4J, K). This strict
399 correspondence between fruit shape and puzzle-shaped epidermal cells fits the prediction of our
400 model that puzzle shapes are required to allow cells to enlarge in isotropically growing tissues, but
401 are not required in elongated organs.

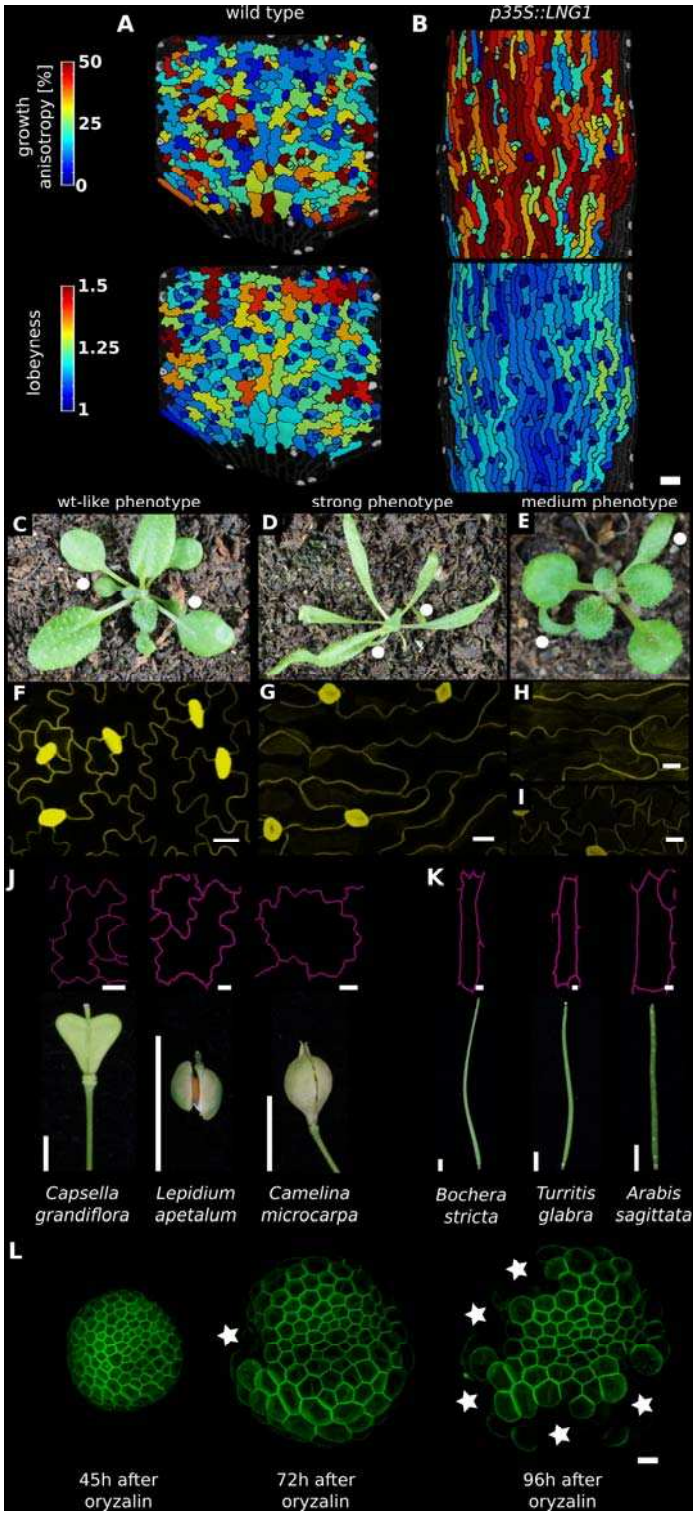

402 **Figure 4. Correlation between growth direction and shape on the cell and organ level.** (A-B)
403 Time-lapse confocal imaging. Pictures were taken every 48 hours and analyzed using
404 MorphoGraphX. The last time point of each series is shown. Growth anisotropy between 2 and 6
405 days after germination (DAG), calculated as the expansion rate in the direction of maximal growth

406 divided by expansion rate in the direction of minimal growth, and cell lobeyness in wildtype (A)
407 and *p35S::LNG1* (B) cotyledons. The *p35S::LNG1* cotyledon displays more anisotropic growth and
408 less lobed epidermal cells. Scale bars: 50 µm. (C-E) *p35S::LNG1* T_1 plants with wild type-like
409 phenotype (C, 61/98 plants), strong phenotype with dramatically elongated cotyledons and leaves
410 (D, 16/98 plants) and intermediate phenotype with elongated cotyledons but wt-like leaves (E,
411 12/98 plants). Cotyledons are marked by white dots. The remaining 9 obtained plants displayed
412 elongated cotyledons and mildly elongated leaves (not shown). (F-I) Confocal images of epidermal
413 cells. Scale bars: 20 µm. (F) shows cells from a leaf in (C), (G) shows cells from a leaf in (D), (H)
414 shows cells from a cotyledon in (E), and (I) shows cells from a leaf in (E). (J-K) Epidermal cell
415 outlines from fruit with more isotropic shapes (silicles, J) and more anisotropic shapes (siliques,
416 K).Fruit images reproduced from figures 4 and S4 of Hofhuis et al. (2016; published under the
417 terms of the Creative Commons Attribution license (http://creativecommons.org/licenses/by/4.0/)).
418 Cell outlines reproduced from Figure 2 of Hofhuis & Hay (2017, adapted with permission from
419 John Wiley and Sons). Scale bars: 10 µm for cell outlines, 1 mm for fruit. (L) Depolymerization of
420 cortical microtubules by oryzalin treatment causes cells of NPA-treated meristems to expand
421 without division, ultimately leading to the rupture of the cell wall due to increased mechanical
422 stress. Regions where cells have ruptured (white stars) are primarily located on the flanks of the
423 meristems, where cells are larger. Scale bar: 20 µm.

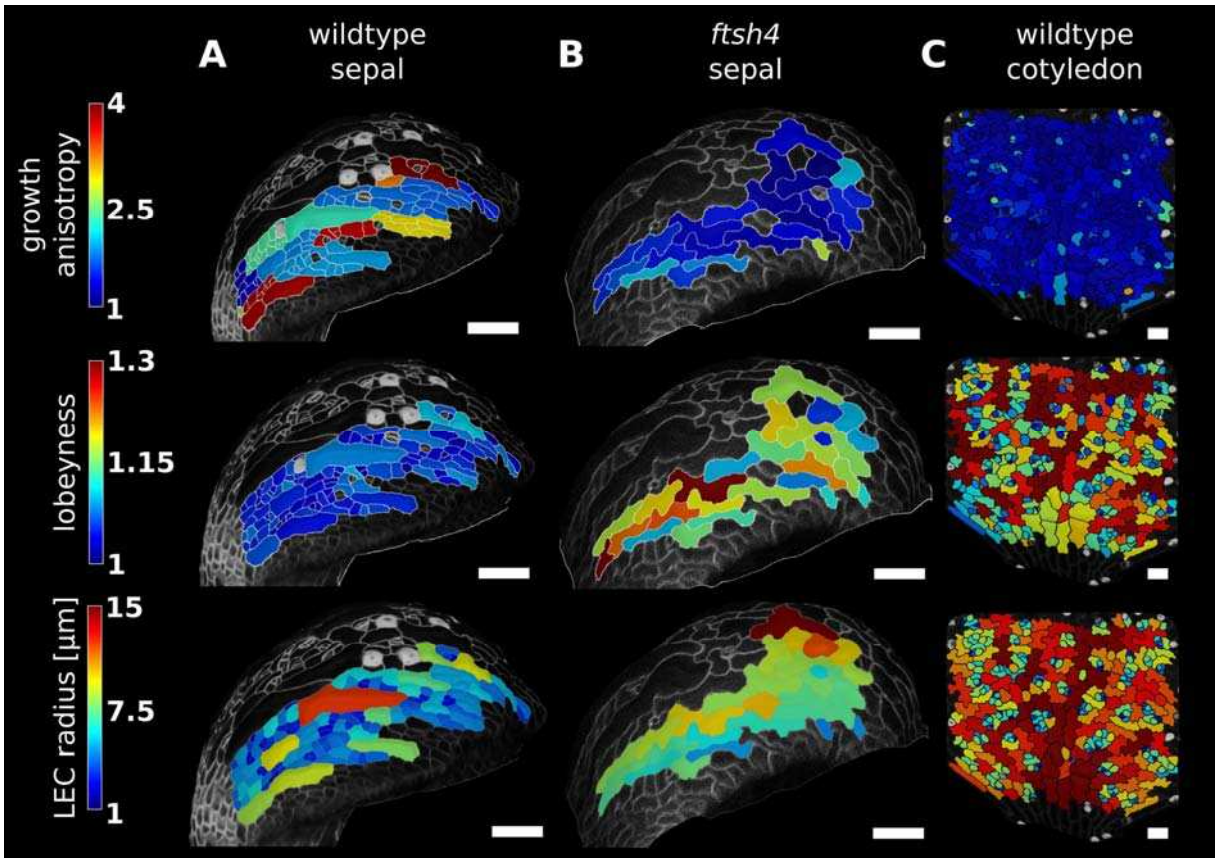

Figure 4 – figure supplement 1. Correlation between growth direction and shape on the cell and organ level demonstrated by time-lapse confocal imaging. Pictures were taken at 24-hour intervals for 3 days (A, wild type sepal; B, *ftsh4* sepal) or 2 days (C, wild type cotyledon) and analyzed using MorphoGraphX. The last time point of each series is shown. Characterization of growth anisotropy (expansion rate in the direction of maximal growth divided by expansion rate in direction of minimal growth) and cell shape (lobeyness and LEC radius) in wildtype sepal, *ftsh4* sepal and the wild type cotyledon, scale bars: 50 µm. Growth patterns of the wild type and *ftsh4* sepals shown were previously described in (Hervieux et al., 2016) and (Hong et al., 2016), respectively.

Lobeyness allows cells to increase their size while avoiding excessive stress

Our model predicts that plant cells regulate their shape to prevent their LEC, a proxy for stress,

436 from becoming too large. To test this hypothesis, we imaged cells of young cotyledons at different
437 stages of growth and tracked changes in cell and LEC area. We reasoned that if the cell area
438 increases faster than LEC area, cells must have a mechanism to maintain a low LEC radius. We
439 imaged 1, 2, 4 and 6 DAG seedlings, as within this time window we could qualitatively observe the
440 most dramatic increase in cellular lobeyness. In the epidermal cells of 2 DAG seedlings, lobes were
441 small or absent in most cells, while 6 days after germination most cells were puzzle-shaped (Fig.
442 5C). For each time point we imaged up to 10 plants and segmented several hundred cells from each
443 plant using MorphoGraphX. We then pooled all cells from each timepoint and calculated average
444 cell area and LEC area for the largest 20% of cells (Fig. 5A, Fig. 5 – Source Data 1).

445 We compared these values to the case where cells are perfectly isodiametric (i.e. circles) so that the
446 cell area and LEC area are equal (Fig. 5A, red line). Our results show that as the cotyledon grows,
447 the ratio of average LEC area to average cell area increases slower than when the cell is circular.
448 Consequently, as organ development progresses, cell area increases faster than LEC area, consistent
449 with the idea that increased lobeyness allows surface area to increase faster than the magnitude of
450 stress (Fig. 5A, blue signs).

451

452 Experimental evidence that stress needs to be managed

453 Our model and experiments show that a mechanism, likely cortical-microtubule dependent,
454 generates puzzle shapes to limit stress in large cells when tissue growth is isotropic. It is commonly
455 observed that the periclinal cell walls slightly bulge out in healthy, turgid cells. However, if stress is
456 indeed a developmental constraint, then when cells grow isotropically without this mechanism, they
457 should bulge excessively, reach their rupture point and burst. The shoot apex of *Arabidopsis* grows
458 isotropically in areas without lateral organs (Kwiatkowska & Dumais 2003; Kierzkowski et al.,
459 2012), with the cells presumably managing their mechanical stress by employing cell division to

460 remain small. In plants grown with auxin transport inhibitor 1-N-naphtylphtalamic acid (NPA), the
461 shoot apex is unable to produce lateral organs, and is uniformly covered in small rapidly dividing
462 cells of isodiametric shape (Reinhardt et al., 2000). Treating these meristems with oryzalin, a
463 chemical compound that depolymerizes cortical microtubules, blocks cell division and anisotropic
464 growth restriction, preventing the formation of puzzle shapes. It has been shown in *Arabidopsis*
465 hypocotyls that oryzalin treatment changes the trajectory of cellulose microfibril-producing
466 molecules (CESA), as there is no organized cortical microtubule array to follow, but does not
467 appear to change the rate of cellulose production (Chan et al., 2010). As such, although oryzalin
468 makes cell walls isotropic by preventing the directionally organized deposition of cellulose, it does
469 not necessarily reduce the overall deposition of cellulose, although this cannot be precluded. Cells
470 of shoot apices in these conditions do not divide, but continue to grow developing large,
471 isodiametric shapes that tend to balloon out (Hamant et al., 2008; Corson et al., 2009).

472 After treating naked meristems of NPA-grown seedlings with oryzalin (5 biological replicates), 20
473 displayed full microtubule depolymerization following oryzalin treatment (as assessed by the
474 absence of cell division). In those 20 samples, we could see cell bursting in the latest time points of
475 13 samples, out of which 10 displayed bursting cells were located in the flank of the meristem,
476 where cell size increased substantially. Although it cannot be completely excluded that these lateral
477 cells, under these experimental conditions, have different wall properties, the most parsimonious
478 explanation is that their cell walls could not withstand the increasing mechanical stress induced by
479 the isotropic expansion. This provides direct experimental support for the proposition that large
480 isodiametrically shaped cells are not viable due to the high stresses on their walls.

481

482 A strategy for when lobes cannot be formed

483 Previous reports have shown that lobe formation in pavement cells is compromised in *spike1*

484 mutants (Qiu et al., 2002). The SPIKE1 protein is a guanine nucleotide exchange factor (GEF) and
485 is required for the production of the active, GTP-bound form of ROP proteins molecular switches
486 that deliver signals to downstream components. SPIKE1 regulates actin polymerization *via* WAVE
487 and ARP2/3 complexes (Basu et al., 2008). Furthermore, it activates ROP2, ROP4 and ROP6,
488 thereby promoting isotropic cell expansion (Ren et al., 2016). Mutant plants have a number of
489 severe phenotypes including reduced trichome branching, altered organ shape and increased
490 sensitivity to low humidity environments. Epidermal cells of *spk1* plants have altered shape, with
491 lobes either small or absent, and compared to wild type, their overall cell shape is much less
492 complicated. Furthermore, the epidermis suffers from defects in cell-cell adhesion, which have been
493 reported to result in gaps between cells that are clearly visible in the cotyledon epidermis from
494 approximately 5 DAG on (Qiu et al., 2002; Ren et al., 2016). It has been reported that *spk1*
495 cotyledons are narrower, but not longer than wild type cotyledons (Qiu et al., 2002) and *spk1* petals
496 display an increase in growth anisotropy at late stages of development, after the general shape of the
497 organ has been established (Ren et al., 2016).

498 In *spk1,* epidermal cells of the cotyledons do not have puzzle-shaped forms (Fig. 5B, D, E, Fig. 5,
499 figure supplement 1B), even though the tissue growth isotropy is similar to wild type plants (n=3
500 time-lapse series, Fig. 4B, Fig. 5, figure supplement 1A – cellular growth anisotropy shows a small
501 statistical difference in that *spk1* grows more anisotropically than wild type). Given our hypothesis
502 that lobes function to reduce mechanical stress (LEC size) during isotropic growth, we tested if
503 LEC was higher in the simple-shaped cells of *spk1* mutant than in the puzzle-shaped cells of wild
504 type. In our time-lapse experiment, even though lobeyness is greatly reduced in *spk1*, LEC radius in
505 the final time point is comparable to wild type (Fig. 5B, Fig. 5, figure supplement 1C). Our FEM
506 simulations revealed that cellular stresses in wild type and *spk1* cells are similar and scale with LEC
507 (compare Fig. 1C and Figure 5 - figure supplement 2). We also performed the same analysis as for
508 wild type, imaging *spk1* cotyledons 1, 2, 4 and 6 DAG and measuring cell area and LEC area (Fig.

509 5C, D). This revealed a similar trend to that observed in the wild type, with cell area increasing
510 faster than LEC area (Fig. 5A) during the course of organ development. At the same time, mean
511 average cell area in *spk1* remained similar or lower than in wild type until 6 DAG (Fig. 5-figure
512 supplement 3). Cells of the *spk1* mutant keep LEC low and overall organ growth remains isotropic.
513 Similar LEC size in mutant and wild type suggests that LEC acts as a threshold for stress based cell
514 shape modification. However, instead of forming lobes, the *spk1* cells themselves seem to
515 interdigitate generating worm-like shapes. It is possible that this strategy is insufficient, as holes
516 appear between cells in the growing epidermis of cotyledons (Fig. 5E), which may be due to
517 increased mechanical stress. However, since holes are already present in cotyledons at 1 DAG it is
518 also possible that they result from direct disruption of the molecular process regulating cellular
519 adhesion, such asactin-driven pectin delivery to cell walls, causing defects prior to the stress-based
520 shape patterning where the final cell shape is established. The *spk1* mutant is unable to make lobes
521 because it fails to activate ROPs which interact with effector proteins to mediate cytoskeletal
522 rearrangements and cell shape (Basu et al., 2008). In our model framework, ROP2 activity would
523 preclude connections where walls have with high curvature, thus preventing connections from
524 penetrating lobes. Apart from removing this assumption from the model, we increased the stiffness
525 of connections and the cell-wall, and decreased the frequency at which connections were reset, to
526 account for defects in ROP-mediated cytoskeletal rearrangement. These three changes to the initial
527 simulation allowed us to reproduce the *spk1* phenotype (Fig. 5F, Movie 4). This suggests that
528 creating interdigitated worm-shaped cells provides an alternate strategy to cover an isotropically
529 growing tissue, although possibly not as efficient in reducing stress as lobe formation.

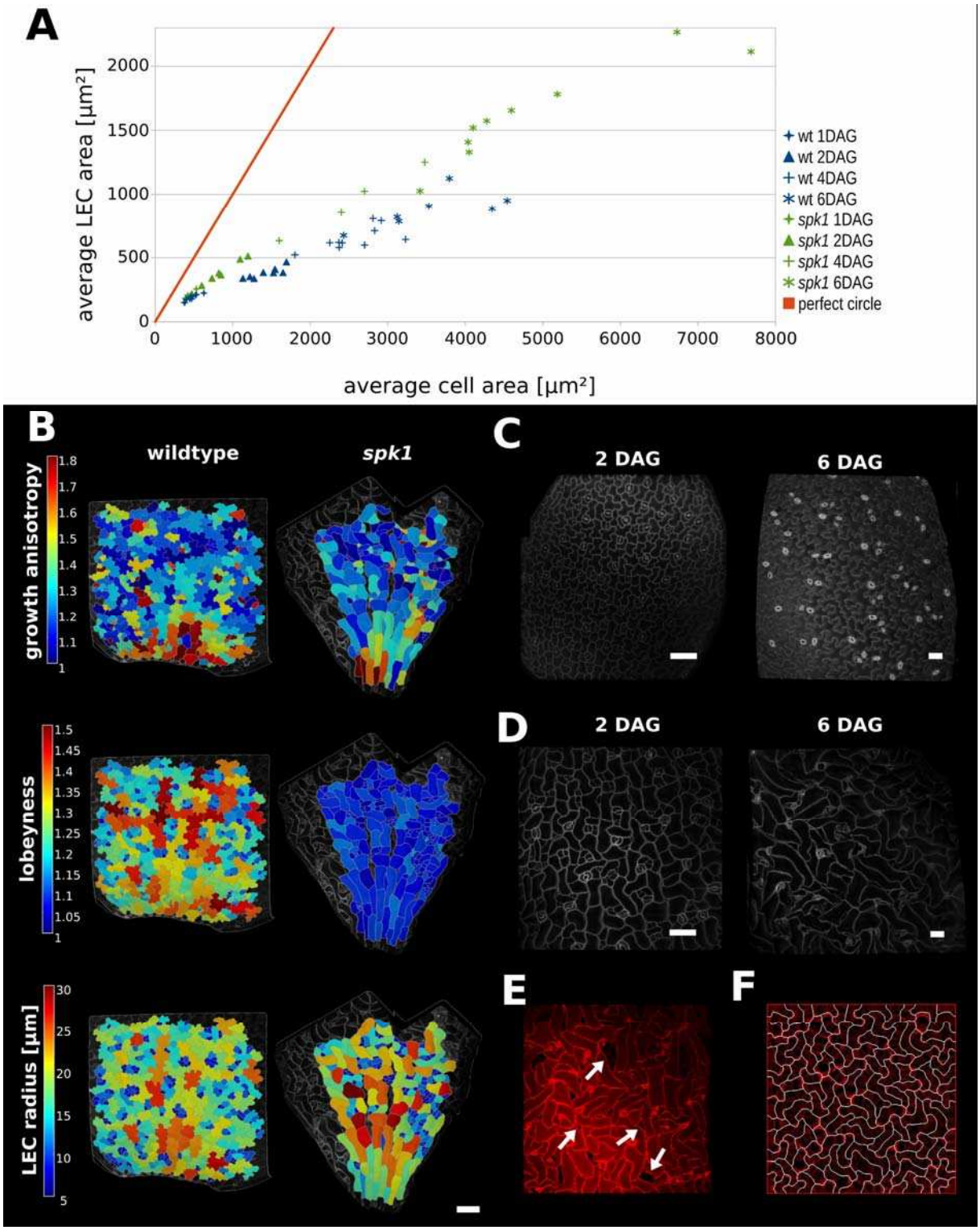

530 **Figure 5. Characterization of *spike1* mutant.** (A) Average LEC area of wild type and *spk1*

531 cotyledons vs. average cell area. The red line represents the theoretical case of a perfectly circular

532 cell. In this case cell area and LEC area increase at the same rate. For the cell area and the LEC area

533 analysis we considered the average values for the largest 20% of segmented cells in order to avoid
534 bias stemming from the much smaller cells of the stomatal lineage, which due to their small size
535 would not need to regulate their LEC. For average values for each point, including sample size and
536 SE, see Fig. 5 – Source Data 1. (B) Time-lapse data on wild type and *spk1* cotyledons. Plants were
537 imaged twice in 48h intervals. Heat maps are displayed on the last time points. Scale bar: 100 µm.
538 (C and D) Examples of cell shapes in the experiment shown in (A). Scale bars: 50 µm. (C) Wild
539 type. (D) *spk1*. (E) Confocal image of *spk1* cotyledon, 8 DAG. Note the gaps between cells and
540 ruptured stomata that typify *spk1* phenotype (some of them indicated by arrows). (F) Model result
541 with increased growth restriction and placement of transverse connections in lobe tips.

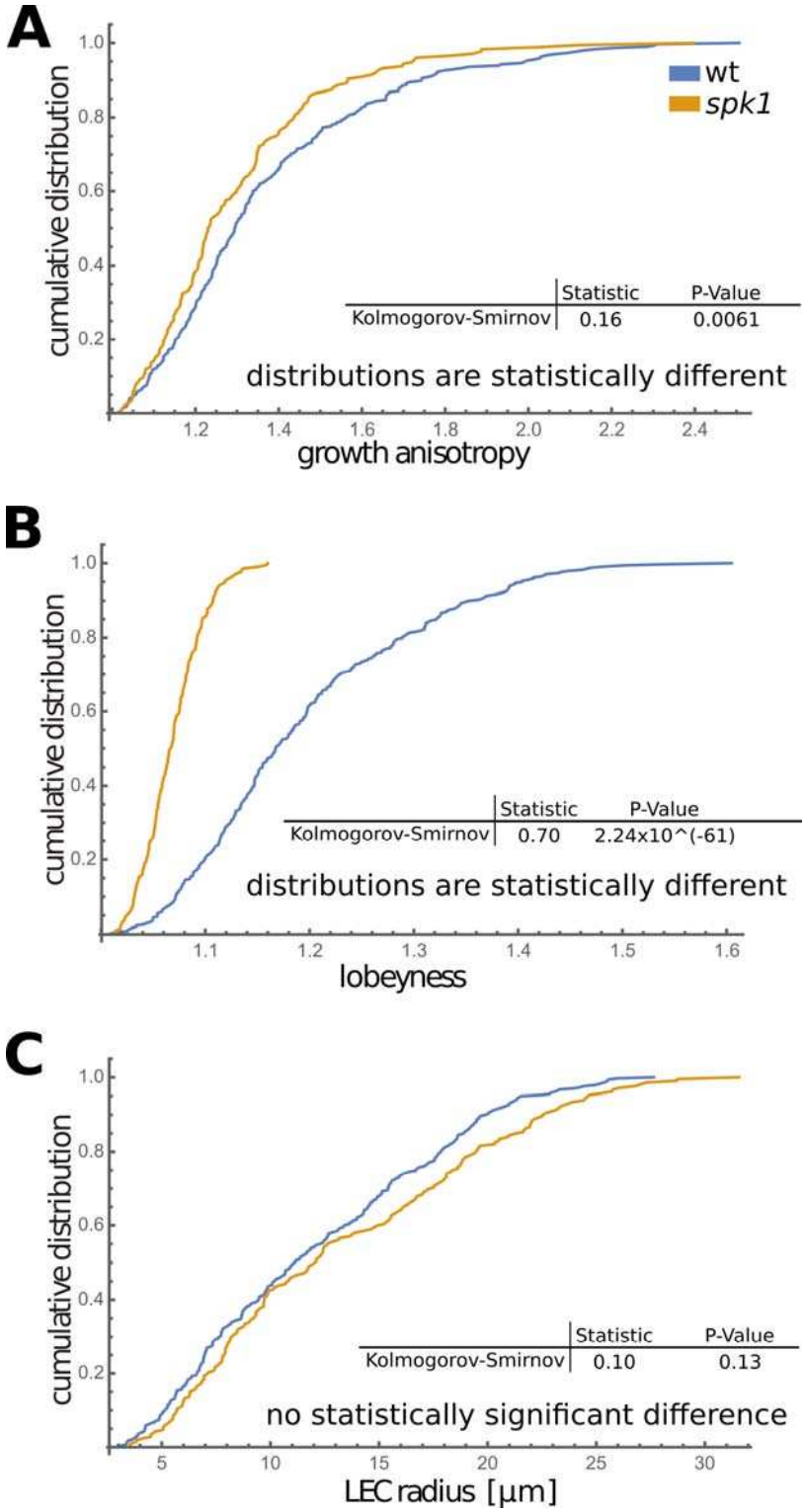

542 **Figure 5 – figure supplement 1. Comparison of growing wt and *spk1* cotyledons.** Correlation

543 distribution of growth anisotropy (A), lobeyness (B) and LEC radius (C) of cells of wild type and

544 *spk1* cotyledons. A Kolmogorov-Smirnov test performed on data from time-lapse imaging

experiments (Fig. 5B) showed that growth anisotropy and cell lobeyness are statistically different in *spk1* compared to wild type (A, B), while there is no statistically significant difference of LEC radius distribution between the two genotypes (C). We consider two distributions different if the p-value is higher than 0.05. This suggests that cells arrive at similar mechanical stress levels (here represented by LEC size) in different ways.

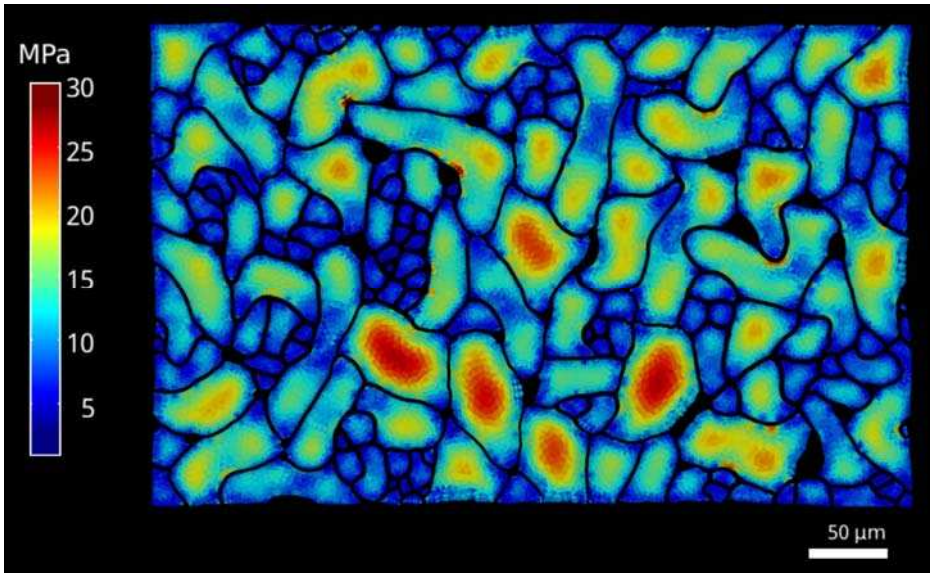

Figure 5 – figure supplement 2. Cellular stress patterns in *spike1* cells. The FEM simulations were performed the same way as the data in Figure 1. Color scale: trace of Cauchy stress tensor in MPa.

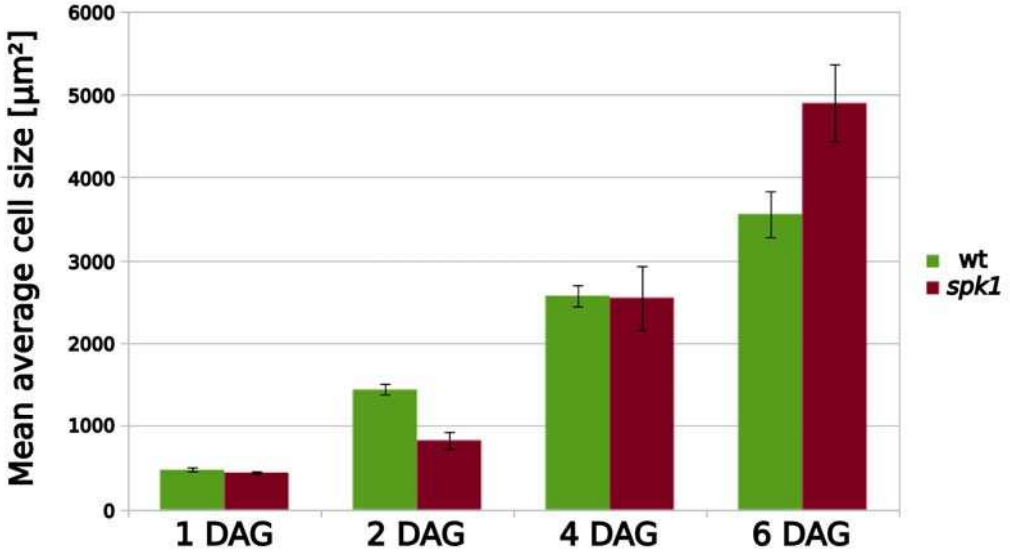

553 **Figure 5 – figure supplement 3. Mean average cell area for wild type and *spk1* cells.** Data
554 obtained from the data displayed in Fig. 5A. For mean average values including SE, please see
555 Figure 5 – Source Data 2.

556

557 ## Cell shape and size across species

558 Our data indicates that the stress control mechanism we propose is conserved between various
559 organs in *A. thaliana*, and within the fruit of Brassicaceae (Fig. 4J, K). This raises the question as to
560 how broadly this mechanism is conserved, with large cell size and isotropic growth correlating with
561 puzzle-shaped cells. Under this assumption, two geometric strategies are possible for cell expansion
562 in isotropically growing organs without requiring excessively thick walls: (1) keeping cell size
563 small by frequent divisions or (2) creating larger, puzzle-shaped cells. We measured cell area, LEC
564 area and lobeyness in the adaxial epidermis of 19 unrelated plant species including trees, shrubs and
565 herbs. A statistical analysis revealed that there was a positive correlation between cell size and
566 lobeyness for each species (Fig. 6A-C). Species with the largest average lobeyness also tended to
567 have the largest cells (and vice-versa, Fig. 6 A-B). For average values of lobeyness and cell area of
568 each species (including sample size), see Figure 6 – Source Data 1. Pearson correlation coefficients

569 ranged from 0.23 for *Catharantus roseus* to 0.94 for *Solanum nigrum* (Fig. 6D). When pooling cells
570 of all species together, the Pearson correlation coefficient was 0.64. Lobe formation is therefore
571 more likely to be observed in big cells rather than small cells, which is intuitive if one considers cell
572 division (where cell size remains low) as an alternative strategy to limit LEC size and cell wall
573 stress. This suggests our hypothesis, that plants create puzzle-shaped cells in order to reduce stress
574 in large isotropically growing cells, may be conserved among many plant species.

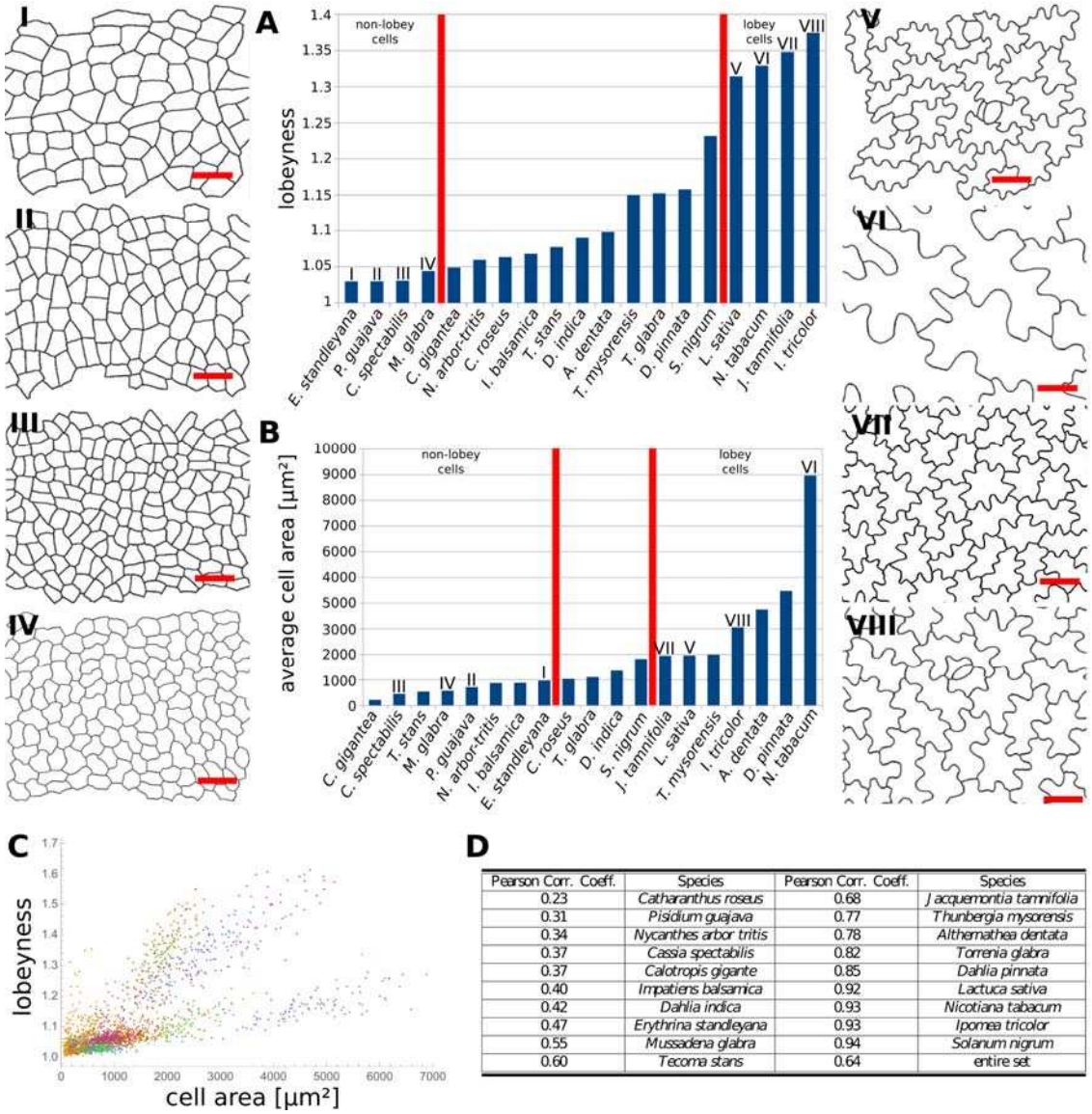

Pearson Corr. Coeff.	Species	Pearson Corr. Coeff.	Species
0.23	*Catharanthus roseus*	0.68	*Jacquemontia tamnifolia*
0.31	*Pisidium guajava*	0.77	*Thunbergia mysorensis*
0.34	*Nycanthes arbor tritis*	0.78	*Althernathea dentata*
0.37	*Cassia spectabilis*	0.82	*Torrenia glabra*
0.37	*Calotropis gigante*	0.85	*Dahlia pinnata*
0.40	*Impatiens balsamica*	0.92	*Lactuca sativa*
0.42	*Dahlia indica*	0.93	*Nicotiana tabacum*
0.47	*Erythrina standleyana*	0.93	*Ipomea tricolor*
0.55	*Mussadena glabra*	0.94	*Solanum nigrum*
0.60	*Tecoma stans*	0.64	entire set

575 **Figure 6**. **Multi-species cell shape analysis.** (A) Average cell lobeyness. (B) Average cell area. (I-
576 VIII) Pictures of leaf epidermal cells of species corresponding to numbering in (A) and (B),

577 numbered by the order of appearance in (A). Scale bars, 50 µm. (C) A plot of lobeyness vs. area for
578 cells of all species pooled together. Each color symbolizes one species. (D) Pearson correlation
579 coefficients between lobeyness and cell area for each species and for all cells pooled together
580 (entire set). Note that in all cases a positive correlation between lobeyness and cell area is observed
581 (correlation coefficient is greater than 0).

582

583 **DISCUSSION**

584 We propose that the puzzle shaped cells seen in the epidermis of many plant species emerge from a
585 mechanism that evolved to limit mechanical stress in tissues that grow isotropically, such as
586 epidermis of leaves and cotyledons. FEM analysis of 3D pressurized cells shows that cell shape
587 influences the direction and magnitude of mechanical stress exerted on the cell wall. When an
588 epidermal cell becomes large in two directions (i.e. has a large open area), stress is greatly
589 increased. In stems, roots and siliques, growth is strongly anisotropic, and cells can simply elongate.
590 This is, however, not possible for isodiametric organs such as broad leaves, cotyledons and silicle
591 fruit pods. We propose that puzzle-shaped cells in the epidermis of more isodiametric plant organs
592 provide a means to avoid large open areas in the cell and the high stresses that they induce. Since
593 turgor pressure inside cells is high, minimizing mechanical stress by shape regulation may be a way
594 of reducing the resources required to reinforce the cell wall and at the same time maintaining its
595 structural integrity during growth.

596 Although it is possible that the interlocking puzzle-shaped cells have a role in strengthening the
597 epidermal cell layer (Glover 2000; Jacques et al., 2014), our experimental data shows that growth
598 anisotropy correlates with cell shape, a prediction that does not appear to readily follow from this
599 alternative hypothesis. Organs displaying isotropic planar growth have puzzle shaped cells while
600 anisotropically growing organs have more elongated cells with fewer lobes. Genetic perturbations

601 that modify growth anisotropy in either direction result in the predicted changes in cell shape. In the
602 *Arabidopsis thaliana* cotyledon, a *p35S::LNG1* overexpression line changes growth from isotropic
603 to anisotropic, and cell shapes become more elongated with fewer lobes. Conversely, in sepals of
604 the *ftsh4* mutant, growth is switched from anisotropic to more isotropic, and the elongated giant
605 cells become more puzzle shaped. Our hypothesis is also consistent with the mild lobing of
606 pavement cells in grass leaves, which often have strongly anisotropic growth (Sylvester et al., 2001)

607 Although studies often focus on anisotropic growth at the cellular level when analyzing puzzle cell
608 development (Armour et al., 2015), our hypothesis suggests that isotropic growth at the tissue level
609 is a primary driver of cell shape. As a tissue grows the stress increases, and microtubules align to
610 direct cellulose deposition to resist the stress. This causes small indentations in the cell, which
611 transfers more stress to them, further recruiting microtubules and more cellulose deposition. The
612 process generates a local activation feedback of cell shape on growth *via* the mechanical stresses
613 that are induced by that shape.

614 A geometric-mechanical simulation model of these processes confirms that the hypothesis is
615 plausible, and the model is able to produce puzzle-shaped cells from a few simple assumptions.
616 Since we use a geometric proxy for stress (LEC), the possibility that the cells sense their geometry
617 through chemical means is also compatible with the model. Our model explains the gradual
618 emergence of lobed cells from polygons resembling meristematic cells, providing an explanation
619 for the till now enigmatic morphogenesis of these distinctive cells. The model suggests that the
620 main driver of the complex puzzle shape comes from the restriction of growth in the indentations,
621 rather than the promotion of growth in the protrusions. It also predicts that the puzzle cell shape is
622 triggered by isotropic growth, and that puzzle cell morphogenesis may not require any signaling
623 molecules to coordinate a protrusion in one cell with the corresponding indentation of its neighbor.
624 Nonetheless, the model does not preclude a role for inter-cellular signaling, which could reinforce
625 patterns produced by geometry sensing or facilitate the initial steps of lobing.

626 The mechanism also predicts that spatial differences in cell wall material properties, corresponding
627 to lobes and indentations, should appear in periclinal cell walls as organized cellulose distributions
628 appear, consistent with observations that cellulose-bundles accumulate in high-stress indentations
629 (Sampathkumar et al., 2014). Spatial differences in stiffness corresponding to incipient lobes and
630 indentations have recently been measured in cross-sections of anticlinal cell walls (Majda et al.,
631 2017). Although the direction of the measurements (z-direction) is not explicitly represented in our
632 model, it is nevertheless consistent with the idea that material properties in adjacent cell walls
633 would be expected to be different in the lobes side vs the indentation side. The modeling results of
634 Majda et al (2017) suggest these mechanical differences drive the formation of small lobes and
635 indentations when the anticlinal walls are placed under tension by turgor pressure. Although this
636 cannot explain deep lobes and indentations or lobes on lobes that emerge in maturing puzzle cells,
637 the idea that both anticlinal cell walls and periclinal cell walls play a coordinated role in puzzle
638 shape morphogenesis (Belteton et al., 2017) is appealing, and warrants further study using FEM
639 models of pavement cell morphogenesis that represent the entire 3D geometry of cells (c.f.
640 Bidhendi and Geitmann, 2017).

641 Our model is also consistent with the functions attributed to the main molecular players that have
642 been reported to influence puzzle cell formation, the ROP family of GTP-ases. The elaboration of
643 puzzle-shape is influenced by two antagonistic molecular pathways. On the convex side
644 (protrusion), ROP2 and ROP4 inactivate the microtubule-associated protein RIC1, thereby
645 suppressing the formation of microtubule arrays, and activate RIC4 which enhances the assembly of
646 actin microfibrils. This was proposed to result in growth promotion (Fu et al., 2005). On the
647 concave side (indentation), ROP6 activates RIC1 and katanin, promoting the formation of bundled
648 microtubule arrays that restrict growth (Fu et al., 2009; Lin et al., 2013). The theory of coordinated
649 outgrowth and restriction has struggled to provide an explanation as to how protrusions and
650 indentations are coordinated between cells. As ROP2 and ROP6 were believed to be activated by

651 auxin (Xu et al., 2010), it was suggested that auxin could act as the mobile signal underlying in this
652 coordination (reviewed by Chen et al., 2015) via ABP1, however this scenario seems unlikely given
653 recent genetic evidence that ABP1 does not have quantifiable effects on auxin response (Gao et al.,
654 2015). Nonetheless, our model is also consistent with the idea that ROP6 is a part of the stress
655 sensing mechanism, and that stress (or strain) is the trigger for localized ROP6 accumulation.
656 Currently, the molecular mechanism for how stress (or strain) could be sensed and its relationship to
657 the ROPs is unknown, although microtubules have been proposed to respond to stress *in planta*
658 (Hejnowicz et al., 2000; Hamant et al., 2008). Since stress is closely related to shape in pressurized
659 plant cells, a curvature sensing mechanism could be involved (Higaki et al., 2016), similar to that
660 proposed for villi patterning during gut morphogenesis (Shyer et al., 2015). Simulations have
661 shown that a ROP2-ROP6 co-repression network can indeed partition a cell in discrete domains of
662 ROP2 and ROP6 expression (Abley et al., 2013). Our data suggest that this intracellular partitioning
663 network works in concert with a mechanical or geometric signal, transmitted by the shape of the
664 cell itself.

665

666

667 # MATERIALS AND METHODS

668 ## Key resources table

Reagent type (species) or resource	Designation	Source or reference	Identifiers	Additional information
gene	*spk1*	Nottingham Arabidopsis Stock Centre	SALK_125206	
genetic reagent	*p35S::LNG1*	this paper		vector obtained using gateway cloning, transformed into Col-0 plants by *Agrobacterium*-mediated floral dipping
genetic reagent	*pUBQ10::myrYFP*	Hervieux et al., 2016		
recombinant DNA reagent	*LNG1* CDS	this paper		Full-length CDS of LONGIFOLIA1 gene, PCR amplified
recombinant DNA reagent	pENTR/D-TOPO	Invitrogen		
recombinant DNA reagent	pK7WG2	Karimi et al., 2002		
genetic reagent	*p35S::LTI6b-GFP*	Cutler et al., 2000		
other	N-(1-naphtyl) phtalamic acid (NPA)	Hamant et al., 2008		
other	oryzalin	Hamant et al., 2008		
software, algorithm	VVE	Smith et al. 2003		www.algorithmicbotany.org
software, algorithm	MorphoGraphX	Barbier de Reuille et al., 2015		www.MorphoGraphX.org

669

670 ## Live imaging of cotyledons

671 Plantlets were grown on 1/2 MS medium in long day conditions as previously described in (Vlad et
672 al., 2014). Young cotyledons (2-6 days after germination, DAG) were imaged using the Leica SP8
673 microscope with 20x (HCX APO, numerical aperture 0.8) and 40x (HCX APO, n.a. 0.5) long
674 working distance, water immersion objectives. Col-0 and *p35S::LNG1* plants contained a plasma
675 membrane-localized fluorescent marker *pUBQ10::myrYFP* previously described in (Hervieux et al.,
676 2016) and fluorescent signal was collected from 519-550 nm emission spectrum using 514 nm laser

677 for excitation. For *spk1* plants and corresponding Col-0 controls, cell walls were stained with
678 propidium iodide and fluorescent signal was collected from 605-644 nm emission spectrum using
679 488 nm laser for excitation. *spk1* homozygous mutant cotyledons were chosen for time-lapse
680 imaging 2 DAG based on their shape which was more elongated compared to wild type cotyledons
681 of comparable age.

682 **Creating transgenic lines**

683 The LNG1 gene full-length CDS was PCR amplified and cloned into the pENTR/D-TOPO vector
684 (Invitrogen) as described in the manual, using primer pair 5'-CACCATGTCGGCGAAGCTTTTGT
685 ATAACT-3' and 5'-GAACATAAGAAAGGGGTTCAGAGA-3'. The resultant vector was LR
686 recombined into the gateway vector pK7WG2 (Karimi et al., 2002) to generate the final construct
687 *p35S::LNG1*. The intermediate and final constructs were verified by sequencing. The *p35S::LNG1*
688 construct was individually transformed into Col-0 plants by *Agrobacterium*-mediated floral dipping.
689 T1 seeds were sown on Kanamycin-containing medium and transferred into soil approximately 2
690 weeks after germination.

691 **Analysis of fruit and exocarp cell shape**

692 Fruit shape was classified as an elongated silique or a silicle (if the length was less than three times
693 the width of the fruit) for 21 species in the Brassicaceae family. Exocarp cells were stained with
694 propidium iodide, imaged by CLSM (as described in section 'Live imaging of cotyledons') and cell
695 outlines extracted using MorphoGraphX.

696 **Time-course imaging of cotyledons**

697 Arabidopsis seeds were sown on a 1/2 MS medium. 1, 2, 4 and 6 days after germination (DAG) 5-
698 10 seedlings were taken out of the medium and imaged. Confocal stacks were processed in
699 MorphoGraphX (Barbier de Reuille et al., 2015). Cell area and LEC radius were calculated for each
700 cell in each sample. For average values displayed in Figure 5A (scatter plot), only the largest 20%
701 of cells in each sample were considered, to eliminate stomata and cells in the stomatal lineage.

702 **Pharmacological treatment**

703 The *p35S::LTI6b-GFP Arabidopsis* lines have been described previously (Cutler et al., 2000) and
704 were grown in tall petri dishes on a on solid custom-made Duchefa "Arabidopsis" medium
705 (DU0742.0025, Duchefa Biochemie) supplemented with 10 µM of NPA (N-(1-naphthyl)
706 phthalamic acid) as described in Hamant et al. (2008). As soon as naked inflorescences had formed,
707 the plants were transferred to a medium without inhibitor. First images (T=0h) were taken 1 day
708 after the plants were taken off the drug. The samples were then immersed for 3h in 20 µg/ml
709 oryzalin at T0h, T24h and T48h, as described in Hamant et al. (2008). Images were acquired using a
710 Leica SP8 confocal microscope. GFP excitation was performed using a 488 nm solid-state laser and
711 fluorescence was detected at 495-535 nm.

712 **Comparison of the distributions of cellular quantities between WT and *spike1***

713 We employed the Kolmogorov-Smirnov (K-S) test to statistically test if the distributions of growth
714 anisotropy, lobeyness and LEC radius between WT and spk1 were the same. We used heat maps
715 created in MorphoGraphX on data displayed in Fig. 5B (final time point) to extract the values for
716 each segmented cell. In the K-S test, the cumulative distribution of the corresponding quantity is
717 first constructed as in Fig. 5, figure supplement 1. The test statistic in the K-S test is the maximum
718 (vertical) distance between the two cumulative distributions from WT and spk1. A large vertical
719 distance signifies that the null hypothesis, i.e., the distributions of WT and spk1 are the same, is
720 more likely to be rejected. The significance level of 0.05 is used in our analysis and we statistically
721 conclude that the two distributions are different if the p-value <0.05.

722 ***spike1* genotyping**

723 The seeds of a heterozygous spk1 T-DNA insertion line (SALK 125206) were purchased from
724 Nottingham Arabidopsis Stock Centre. Segregating individuals were genotyped according to
725 instructions provided by the SALK institute (http://signal.salk.edu/) using primers 5'-
726 GATTTCAGTCTCTCACCGCAG-3' and 5'-ATGGTCGACTCCACATTTCTG-3' for detecting

727 individuals with no T-DNA insertion and primers 5'-ATTTTGCCGATTTCGGAAC-3'
728 (recommended by SALK) and 5'-ATGGTCGACTCCACATTTCTG-3' for detecting individuals
729 containing the T-DNA insertion (mutant plants).

730 **Multi-species leaf cell shape analysis**

731 Leaf surface impressions were taken from the adaxial side using transparent nail enamel (Revlon).
732 The impressions were viewed under the differential interference contrast (DIC) mode of an
733 Olympus BX52a upright microscope (Olympus, Japan) and imaged using a CapturePro CCD
734 camera (Jenoptik, Germany). Images were loaded into MorphoGraphX and cell outlines were
735 projected on a flat (2D) mesh. The mesh was segmented, cell area, lobeyness and LEC radius were

736 **Lobeyness and Largest Empty Circle**

737 The Lobeyness and Largest Empty Circle (LEC) measures are calculated using custom plugins
738 developed for MorphoGraphX (Barbier de Reuille et al., 2015). These measures are applied to 2D
739 cell contours, obtained by projecting each 3D cell-contour extracted using MorphoGraphX on a
740 local plane. For this purpose, the plane minimizing the loss of variance following projection is used.
741 This plane is obtained from Principal Component Analysis (PCA) of the contour points, and is
742 defined as the plane orthogonal to the third principal component (i.e. the direction of minimal
743 variance) passing through the mean of the contour. Lobeyness captures the deviation of 2D cell
744 contours from the convex polygonal forms typical of young undifferentiated cells. The measure is
745 computed by taking the ratio of the cell's perimeter to that of its convex hull (the smallest convex
746 shape containing the cell), and is the inverse of the convexity measure used in Wu et al. (2016).
747 Lobeyness takes a value of 1 for convex shapes and increases with contour complexity. This
748 provides a translation, scale and rotation invariant measure of contour complexity and overall
749 pavement cell lobation. The LEC for each cell is computed using the Delaunay triangulation of the
750 contour positions. The cell contour defines a bounded region of the plane, and the largest empty
751 circle within this region must be either the circumscribed circle of a triangle in the Delaunay

752 triangulation, or a point on the boundary (Toussaint, 1983). Thus, the LEC for each cell is
753 calculated by:
754 1. Computing the Delaunay triangulation of the projected cell-contour.
755 2. Calculating the radii for the circumscribing circle of each triangle within the cell.
756 3. Returning the radius of the largest circle.
757 As the cell-contours extracted from MorphoGraphX are densely sampled compared to the size of
758 cells, the possibility that the largest empty space corresponds to a point on the boundary is ignored.
759

760 **ACKNOWLEDGEMENTS**

761 We thank Arezki Boudaoud for discussions. Funding for this research is gratefully acknowledged
762 from the Swiss National Science Foundation SystemsX.ch iPhD grant 2010/073 to R.S.S., the
763 Bundesministerium für Bildung und Forschung grants 031A492 and 031A494 to R.S.S, Human
764 Frontiers Science Program grant RGP0008/2013 to A.H.K.R, C.B.L., O.H, and R.S.S., the
765 European Commission through a Marie Skłodowska-Curie individual fellowship (Horizon 2020,
766 703886) to A.R., Natural Sciences and Engineering Research Council of Canada Discovery Grant
767 RGPIN-2014-05325 to P.P., European Research Council grant ERC-2013-CoG-615739
768 ‘‘MechanoDevo’’ to O.H., and a core grant from the Max Planck Society to M.T.
769

770 **REFERENCES**

771 **Abley, K., Reuille, P.B. De, Strutt, D., Bangham, A., Prusinkiewicz, P., Marée, A.F.M.,**
772 **Grieneisen, V.A., and Coen, E.** (2013). An intracellular partitioning-based framework for
773 tissue cell polarity in plants and animals. **2074**: 2061–2074.

774 **Armour, W.J., Barton, D. a., Law, A.M.K., and Overall, R.L.** (2015). Differential growth in
775 periclinal and anticlinal walls during lobe formation in *Arabidopsis* cotyledon pavement cells.

776 Plant Cell **27**: 2484–2500.

777 **Barbier de Reuille, P., Routier-Kierzkowska, A.-L., Kierzkowski, D., Bassel, G. W.,**
778 **Schüpbach, T., Tauriello, G., Bajpai, N., Strauss, S., Weber, A., Kiss, A. et al.** (2015).
779 MorphoGraphX: a platform for quantifying morphogenesis in 4D. eLife **4**: 1–20.

780 **Bassel, G.W., Stamm, P., Mosca, G., Barbier de Reuille, P., Gibbs, D.J., Winter, R., Janka, A.,**
781 **Holdsworth, M.J., and Smith, R.S.** (2014). Mechanical constraints imposed by 3D cellular
782 geometry and arrangement modulate growth patterns in the *Arabidopsis* embryo. Proc. Natl.
783 Acad. Sci. **111**: 8685-8690.

784 **Basu, D., Le, J., Zakharova, T., Mallery, E.L., and Szymanski, D.B.** (2008). A SPIKE1
785 signaling complex controls actin-dependent cell morphogenesis through the heteromeric
786 WAVE and ARP2 / 3 complexes. Proc. Natl. Acad. Sci. U. S. A. **105**: 4044–4049.

787 **Beauzamy, L., Louveaux, M., Hamant, O., and Boudaoud, A.** (2015). Mechanically, the shoot
788 apical meristem of *Arabidopsis* behaves like a shell inflated by a pressure of about 1 MPa.
789 Front. Plant Sci. **6**: 1–10.

790 **Belteton, S. A., Sawchuk, M.G., Donohoe, B.S., Scarpella, E. and Szymanski, D.B.** (2017).
791 Reassessing the roles of PIN proteins and anticlinal microtubules during pavement cell
792 morphogenesis. Plant Phys.: pp-01554.

793 **Besson, S. and Dumais, J.** (2011). Universal rule for the symmetric division of plant cells. Proc.
794 Natl. Acad. Sci. U. S. A. **108**: 6294-6299.

795 **Bidhendi, A. and Geitmann, A.** (2017). Finite element modeling of shape changes in plant cells.
796 Plant Phys.: pp. 01684.2017

797 **Chan, J., Crowell, E., Eder, M., Calder, G., Bunnewell, S., Findlay, K., Vernhettes, S., Hoefte,**
798 **H., Loyd, C.** (2010). The rotation of cellulose synthase trajectories is microtubule dependent

799 and influences the texture of epidermal cell walls in *Arabidopsis* hypocotyls. Journal of Cell
800 Science **123**: 3490-3495.

801 **Chen, J., Wang, F., Zheng, S., Xu, T., and Yang, Z.** (2015). Pavement cells: a model system for
802 non-transcriptional auxin signalling and crosstalks. J. Exp. Bot. **66**: 4957–4970.

803 **Corson, F., Hamant, O., Bohn, S., Traas, J., Boudaoud, A., and Couder, Y.** (2009). Turning a
804 plant tissue into a living cell froth through isotropic growth. Proc. Natl. Acad. Sci. U. S. A.
805 **106**: 8453–8.

806 **Cosgrove, D.J.** (2005). Growth of the plant cell wall. Nature **6**: 850-61.

807 **Cosgrove, D.J.** (2014). Re-constructing our models of cellulose and primary cell wall assembly.
808 Curr. Op. in Plant Biol. **22**: 122–131.

809 **Cutler, S. R., Erhardt, D. W., Griffitts, J. S. and Sommerville, C. R.** (2000). Random
810 GFP::cDNA fusions enable visualization of subcellular structures in cells of *Arabidopsis* at a
811 high frequency. Proc. Natl. Acad. Sci. U. S. A. **97**: 3718-3723.

812 **Drevensek, S., Goussot, M., Duroc, Y., Christodoulidou, A., Steyaert, S., Schaefer, E.,**
813 **Duvernois, E., Grandjean, O., Vantard, M., Bouchez, D. and Pastuglia, M.** (2012). The
814 *Arabidopsis* TRM1-TON1 interaction reveals a recruitment network common to plant cortical
815 microtubule arrays and eukaryotic centrosomes. The Plant Cell **24**: 178-191.

816 **Eldridge, T., Łangowski, Ł., Stacey, N., Jantzen, F., Moubayidin, L., Sicard, A., Southam, P.,**
817 **Kennaway, R., Lenhard, M., Coen, E.S., et al.** (2016). Fruit shape diversity in the
818 Brassicaceae is generated by varying patterns of anisotropy. Development **143**: 3394–3406.

819 **Forouzesh, E., Goel, A., Mackenzie, S.A., and Turner, J.A.** (2013). In vivo extraction of
820 *Arabidopsis* cell turgor pressure using nanoindentation in conjunction with finite element
821 modeling. Plant J. **73**: 509–520.

822 **Franks, P.J., Buckley, T.N., Shope, J.C., and Mott, K.A.** (2001). Guard cell volume and pressure
823 measured concurrently by confocal microscopy and the cell pressure probe. Plant Physiol. **125**:
824 1577–1584.

825 **Fu, Y., Gu, Y., Zheng, Z., Wasteneys, G., and Yang, Z.** (2005). *Arabidopsis* interdigitating cell
826 growth requires two antagonistic pathways with opposing action on cell morphogenesis. Cell
827 **120**: 687–700.

828 **Fu, Y., Li, H., and Yang, Z.** (2002). The ROP2 GTPase controls the formation of cortical fine f-
829 actin and the early phase of directional cell expansion during *Arabidopsis* organogenesis. Plant
830 Cell **14**: 777–794.

831 **Fu, Y., Xu, T., Zhu, L., Wen, M., and Yang, Z.** (2009). A ROP GTPase signalling pathway
832 controls cortical microtubule ordering and cell expansion in *Arabidopsis*. Curr. Biol. **19**: 1827–
833 1832.

834 **Gao, Y., Zhang, Y., Zhang, D., Dai, X., Estelle, M., and Zhao, Y.** (2015). Auxin binding protein
835 1 (ABP1) is not required for either auxin signaling or *Arabidopsis* development. Proc. Natl.
836 Acad. Sci. U. S. A. **112**: 2275–2280.

837 **Geitmann, A. and Ortega, J.K.E.** (2009). Mechanics and modeling of plant cell growth. Trends
838 Plant Sci. **14**: 467–478.

839 **Glover, B.J.** (2000). Differentiation in plant epidermal cells. J. Exp. Bot. **51**: 497–505.

840 **Green, P.B.** (1962). Mechanism for plant cellular morphogenesis. Science. **138**: 1404–1405.

841 **Hamant, O., Heisler, M.G., Jönsson, H., Krupinski, P., Uyttewaal, M., Bokov, P., Corson, F.,**
842 **Sahlin, P., Boudaoud, A., Meyerowitz, E.M., et al.** (2008). Developmental patterning by
843 mechanical signals in *Arabidopsis*. Science **322**: 1650–1655.

844 **Hejnowicz, Z., Rusin, A., and Rusin, T.** (2000). The orientation of cortical microtubules in the

845 epidermis of sunflower hypocotyl. J. Plant Growth Regul. **19**: 31–44.

846 **Hervieux, N., Dumond, M., Sapala, A., Routier-Kierzkowska, A.-L., Kierzkowski, D., Roeder,**
847 **A.H.K., Smith, R.S., Boudaoud, A., and Hamant, O.** (2016). A mechanical feedback
848 restricts sepal growth and shape in *Arabidopsis* a mechanical feedback restricts sepal growth
849 and shape in *Arabidopsis*. Curr. Biol. **26**: 1019–1028.

850 **Higaki, T., Kutsuna, N., Akita, K., Takigawa-Imamura, H., Yoshimura, K. and Miura, T.**
851 (2016). A theoretical model of jigsaw-puzzle pattern formation by plant leaf epidermal cells.
852 PLOS Computational Biology **12**: e1004833.

853 **Hofhuis, H. and Hay, A.** (2017). Explosive seed dispersal. New Phytologist. **216**: 339-342.

854 **Hofhuis, H., Moulton, D., Lessinnes, T., Routier-Kierzkowska, A.-L., Bomphrey, R. J., Mosca,**
855 **G., Reinhardt, H., Sarchet, P., Gan, X., Tsiantis, M. et al.** (2016). Morphomechanical
856 innovation drives explosive seed dispersal. Cell **166**: 222–233.

857 **Hong, L., Dumond, M., Tsugawa, S., Sapala, A., Routier-Kierzkowska, A.-L., Zhou, Y., Chen,**
858 **C., Kiss, A., Zhu, M., Hamant, O. et al.** (2016). Variable cell growth yields reproducible
859 organ development through spatiotemporal averaging. Dev. Cell **38**: 15–32.

860 **Jacques, E., Verbelen, J.-P., and Vissenberg, K.** (2014). Review on shape formation in epidermal
861 pavement cells of the Arabidopsis leaf. Functional Plant Biology **41**: 914-921.

862 **Karimi, M., Inze, D. and Depicker, A.** (2002). GATEWAY vectors for *Agrobacterium*-mediated
863 plant transformation. Trends in Plant Sci. **7(5)**: 193–195.

864 **Kierzkowski, D., Nakayama, N., Routier-Kierzkowska, A.-L., Weber, A., Bayer, E.,**
865 **Schorderet, M., Reinhardt, D., Kuhlemeier, C., and Smith, R.S.** (2012). Elastic domains
866 regulate growth and organogenesis in the plant shoot apical meristem. Science **335**: 1096–
867 1099.

868 **Kutschera, U. and Niklas, K.J.** (2007). The epidermal-growth-control theory of stem elongation:
869 An old and a new perspective. J. Plant Physiol. **164**: 1395–1409.

870 **Kwiatkowska, D. and Dumais, J.** (2003). Growth and morphogenesis at the vegetative shoot apex
871 of *Anagallis arvensis* L. J. Exp. Bot. **54**: 1585–1595.

872 **Le, J., Mallery, E.L., Zhang, C., Brankle, S. and Szymanski, D.B.** (2006). *Arabidopsis* BRICK1
873 / HSPC300 is an essential WAVE-complex subunit that selectively stabilizes the Arp2 / 3
874 activator SCAR2. Curr. Biol. **16**: 895–901.

875 **Lee, Y.K., Kim, G.-T., Kim, I.-J., Park, J., Kwak, S.-S., Choi, G., and Chung, W.-I.** (2006).
876 LONGIFOLIA1 and LONGIFOLIA2, two homologous genes, regulate longitudinal cell
877 elongation in *Arabidopsis*. Development **133**: 4305–4314.

878 **Lee, G.Y, Cheung, K., Chang, W., Lee, L.P.** (2000). Mechanical interlocking with precisely
879 controlled nano- and microscale geometries for implantable microdevices. 1st Annu. Int.
880 IEEE-EMBS Spec. Top. Conf. Microtechnologies Med. Biol.

881 **Li, H., Lin, D., Dhonukshe, P., Nagawa, S., Chen, D., Friml, J., and Scheres, B.** (2011).
882 Phosphorylation switch modulates the interdigitated pattern of PIN1 localization and cell
883 expansion in *Arabidopsis* leaf epidermis. Nature **21**: 970–978.

884 **Lin, D., Cao, L., Zhou, Z., Zhu, L., Ehrhardt, D., Yang, Z., and Fu, Y.** (2013). Rho GTPase
885 signaling activates microtubule severing to promote microtubule ordering in *Arabidopsis*.
886 Curr. Biol. **23**: 290–297.

887 **Lloyd, C.W.** (1991). How does the cytoskeleton read the laws of geometry in aligning the division
888 plane of plant cells? Development Supplement **1**: 55-56.

889 **Majda, M., Grones, P, Sintorn, I.-M., Vain, T., Milani, P., Krupinski, P., Zagorska-Marek, B.,**
890 **Viotti, C., Jönsson, H., Mellerowicz, E. J., Hamant, O., Robert, S.** (2017).

Mechanochemical polarization of contiguous cell walls shapes plant pavement cells. Dev. Cell **43**: 290-304.

Matthews, M. (2002). Physically based simulation of growing tissues. Master's thesis, University of Calgary.

Mosca, G., Sapala, A., Strauss, S., Routier-Kierzkowska A.-L., Smith, R.S. (2017). On the micro-indentation of plant cells in a tissue context. Phys. Biol. **14:** 015003.

Mosca, G., Adibi, M., Strauss, S., Runions, A., Sapala, A. and Smith, R.S. (2018). Modeling plant tissue growth and cell division. To appear in Mathematical Modeling in Plant Biology (Springer Verlag).

Nakielski J. (2000). Tensorial model for growth and cell division in the shoot apex. In Pattern Formation in Biology, Vision and Dynamics, A. Carbone, M. Gromov, P. Prusinkiewicz, Eds. (World Scientific), pp. 252-286.

Niklas, K.J. (1992). Plant Biomechanics: An Engineering Approach to Plant Form and Function (The University of Chicago Press).

Paredez, A.R., Somerville, C.R. and Erhardt, D.W. (2006). Visualization of cellulose synthase demonstrates functional association with microtubules. Science **312**: 1491-1495.

Prusinkiewicz P. and Lindenmayer, A. (1990). The Algorithmic Beauty of Plants (Springer, New York).

Qiu, J.-L., Jilk, R., Marks, M.D., and Szymanski, D.B. (2002). The *Arabidopsis* SPIKE1 gene is required for normal cell shape control and tissue development. Plant Cell **14**: 101–118.

Reinhardt, D., Mandel, T., and Kuhlemeier, C. (2000). Auxin regulates the initiation and radial position of plant lateral organs. Plant Cell **12**: 507–18.

Ren, H., Dang, X., Yang, Y., Huang, D., Liu, M., Gao, X., and Lin, D. (2016). SPIKE1 activates

914 ROP GTPase to modulate petal growth and shape. Plant Physiol. **172**: 358–371.

915 **Richards, O.W., and Kavanagh, A.J.** (1943). The analysis of the relative growth gradients and
916 changing form of growing organisms: illustrated by the tobacco leaf. The American Naturalist
917 **77**: 385–399.

918 **Sampathkumar, A., Krupinski, P., Wightman, R., Milani, P., Berquand, A., Boudaoud, A.,**
919 **Hamant, O., Jönsson, H., and Meyerowitz, E.M.** (2014). Subcellular and supracellular
920 mechanical stress prescribes cytoskeleton behavior in *Arabidopsis* cotyledon pavement cells.
921 Elife **3**: e01967.

922 **Savaldi-Goldstein, S., Peto, C., and Chory, J.** (2007). The epidermis both drives and restricts
923 plant shoot growth. Nature **446**: 199–202.

924 **Shyer, A.E., Huycke, T. R., Lee, C.H., Mahadevan, L. and Tabin, C. J.** (2015). Bending
925 gradients : how the intestinal stem cell gets its home. Cell **161**: 569–580.

926 **Smith, C., Prusinkiewicz P. and Samavati F.** (2003). Local specification of surface subdivision
927 algorithms. In Proceedings of AGTIVE 2003, Lecture Notes in Computer Science, vol. 3062,
928 Springer, pp. 313-327.

929 **Sotiriou, P., Giannoutsou, E., Panteris, E., Galatis, B. and Apostolakos, P.** (2018), Local
930 differentiation of cell wall matrix polysaccharides in sinuous pavement cells: its possible
931 involvement in the flexibility of cell shape. Plant Biol J.

932 **Suslov, D. and Verbelen, J.** (2006). Cellulose orientation determines mechanical anisotropy in
933 onion epidermis cell walls. J. Exp. Bot. **57**: 2183–2192.

934 **Sylvester, A.W., Parker-Clark, V., Murray, G.A.** (2001). Leaf shape and anatomy as indicators
935 of phase change in the grasses: comparizon of maize, rice and bluegrass. Am. J. Bot. **88**: 2157-
936 2167.

Toussaint, G. T. (1983). Computing largest empty circles with location constraints. International Journal of Parallel Programming **12**: 347–358.

Vlad, D., Kierzkowski, D., Rast, M. I., Vuolo, F., Dello Ioio, R., Calinha, C., Gan, X., Hajdehari, M., Hay, A., Smith, R.S. et al. (2014). Leaf shape evolution through duplication, regulatory diversification, and loss of a homeobox gene. Science. **343**: 780-783.

Wang, Y., Xiong, G., Hu, J., Jiang, L., Yu, H., Xu, J., Fang, Y.,Zeng, L., Xu, E., Xu, J. et al. (2015). Copy number variation at the GL7 locus contributes to grain size diversity in rice. Nat. Gen. **47**: 944-948.

Wu, T.-C., Belteton, S. A., Pack, J., Szymanski, D. B., Umulis, D.M. (2016). LobeFinder: a convex hull-based method for quantitative boundary analyses of lobed plant cells. Plant Physiol. **171**: 2331–2342.

Xu, T., Wen, M., Nagawa, S., Fu, Y., Chen, J., Wu, M.-J., Perrot-Rechenmann, C., Friml, J., Jones, A.M., and Yang, Z. (2010). Cell surface- and Rho GTPase-based auxin signalling controls cellular interdigitation in *Arabidopsis*. Cell **143**: 99–110.

Zhang, C., Halsey, L.E., and Szymanski, D.B. (2011). The development and geometry of shape change in *Arabidopsis* thaliana cotyledon pavement cells. BMC Plant Biol. **11**:27.

SUPPLEMENTARY FILES

Appendix. Modeling supplement. Contains technical details regarding 3D Finite Element Method modeling and 2D tissue growth model.

Movie 1. Simulation of cell shape development in an isotropically expanding tissue. The tissue is shown at two scales: unscaled (Left) and scaled to maintain a constant tissue width (Right). Red lines traversing cell-interiors correspond to active growth restrictions. Scale bar indicates a constant

960 reference length of arbitrary value.

961 **Movie 2. Simulation of cell shape development in an anisotropically expanding tissue.** The
962 tissue is shown at two scales. (Left) Scaled to maintain a constant tissue width. (Right) Scaled so
963 that the largest dimension of the tissue is constant. Scale bars indicate a common constant reference
964 length of arbitrary value.

965 **Movie 3. Simulation of cell shape development in an non-uniformly expanding tissue.** Growth
966 anisotropy increases linearly from the left to right. The tissue is shown at two scales: unscaled
967 (Left) and scaled to maintain a constant tissue width (Right). Red lines traversing cell-interiors
968 correspond to active growth restrictions. Scale bar indicates a constant reference length of arbitrary
969 value.

970 **Movie 4. Simulation of the development of *spk1*-like cells in an isotropically expanding tissue.**
971 The tissue is shown at two scales: unscaled (Left) and scaled to maintain a constant tissue width
972 (Right). Red lines traversing cell-interiors correspond to active growth restrictions. Scale bar
973 indicates a constant reference length of arbitrary value.

974 **Movie 5. Simulation results when growth isotropy is varied.** Using the wild type isotropic
975 simulation as a reference, growth isotropy (growth in width/growth in height, or g_x/g_y in Appendix)
976 is varied from 50% to 100% of the reference value in regular increments. Successive frames show
977 the final stage of each simulation as isotropy is increased. Scale bars indicate a constant reference
978 length.

979 **Movie 6. Simulation results when bending stiffness is varied.** Using the wild type isotropic
980 simulation as a reference, bending stiffness (k_b in Appendix) is varied with respect to the reference
981 value from 5% to 25% and then from 25%-200% by increments of 25%. Successive frames show
982 the final stage of each simulation as the bending stiffness is increased. Scale bars indicate a constant
983 reference length.

984 **Movie 7. Simulation results when cellulose stiffness is varied.** Using the wild type isotropic

985 simulation as a reference, cellulose stiffness (k_m in Appendix) is varied with respect to the reference
986 value from 0%-200% by increments of 25%. Successive frames show the final stage of each
987 simulation as the cellulose stiffness is increased. Scale bars indicate a constant reference length.
988 **Movie 8. Simulation results when stretching stiffness is varied.** Using the wild type isotropic
989 simulation as a reference, stretching stiffness (k_s in Appendix) is varied with respect to the reference
990 value from 25%-200% by increments of 25%. Successive frames show the final stage of each
991 simulation as the stretching stiffness is increased. Scale bars indicate a constant reference length.
992 **Movie 9. Simulation results when target LEC is varied.** Using the wild type isotropic simulation
993 as a reference, target LEC (min_{micro} in Appendix) is varied with respect to the reference value from
994 0%-200% by increments of 25%. Successive frames show the final stage of each simulation as the
995 target LEC is increased. Scale bars indicate a constant reference length.
996 **Movie 10. Simulation results when normal angle is varied.** Using the wild type isotropic
997 simulation as a reference, normal angle (θ_{micro} in Appendix) is varied with respect to the reference
998 value from 25%-200% by increments of 25%. Successive frames show the final stage of each
999 simulation as the normal angle is increased. Scale bars indicate a constant reference length.
1000 **Figure 5 – Source Data 1.** Average cell area and LEC area for wt and *spk1* cotyledon time-course.
1001 This table contains average values for 20% largest segmented cells (in each sample), displayed in
1002 Fig. 5A.

1003 **Figure 5 – Source Data 2.** Mean average cell area for wild type and *spk1* cotyledon cells (20%
1004 largest segmented cells for each sample, averaged), displayed in Figure 5 – figure supplement 3.

1005 **Figure 6 – Source Data 1.** Average cell area and lobeyness for all studied species. Number of cells
1006 measured for each species, average values and SE are included.

1007 **Figure supplements (captions embedded in the text alongside primary figures):**

1008 **Figure 2 – figure supplement 1.** Mechanical properties of the cell wall are simulated using

1009 stretching and bending springs.

1010 **Figure 3 – figure supplement 1.** Parameter space exploration for key model parameters.

1011 **Figure 4 – figure supplement 1.** Correlation between growth direction and shape on the cell and

1012 organ level demonstrated by time-lapse confocal imaging.

1013 **Figure 5 – figure supplement 1.** Comparison of growing wt and *spk1* cotyledons.

1014 **Figure 5 – figure supplement 2.** Cellular stress patterns in *spike1* cells.

1015 **Figure 5 – figure supplement 3.** Mean average cell area for wild type and *spk1* cells.

1016

1017